

Ab Initio and Empirical Model MD Simulation Studies of Solvent Effects on the Properties of *N*-Methylacetamide along a *cis*–*trans* Isomerization Pathway

Yves A. Mantz,^{*,†} Helene Gerard,[‡] Radu Iftimie,^{§,||} and Glenn J. Martyna[†]

IBM T.J. Watson Research Laboratory—Yorktown, Route 134 & PO Box 218,
Yorktown Heights, New York 10598-0218, Laboratoire de Chimie Théorique,
Université Pierre et Marie Curie, Tour 22-23, 1er étage, Case 137, 4 place Jussieu, 75252 Paris, France,
Department of Chemistry, New York University, New York, New York, 10003-6688

Received: February 16, 2006; In Final Form: April 20, 2006

The properties of *N*-methylacetamide along a *cis*–*trans* isomerization pathway described by twisting about the C(O)–N bond are examined at finite temperature both in vacuo and in explicit water solvent. Two distinctly different theoretical descriptions, an ab initio (DFT-BLYP) and an empirical (CHARMM22) model, are studied in order to permit an assessment of the dominant forces active in the system. An analysis of the solvent structure at equilibrium and changes in solvation structure accompanying isomerization is, therefore, given for each model. Many-body polarization effects absent under CHARMM22 but present in the ab initio model are found to have a profound influence on the system. The electronic structure of the NMA molecule predicted by the ab initio method along the reaction coordinate is examined in order to shed further light on changes in peptide “partial-double” bond character [C(O)–N] as isomerization takes place. A new statistical-mechanical interpretation of the entropy change during a chemical reaction is presented to help interpret the thermochemistry of the simple reaction.

I. Introduction

N-Methylacetamide (NMA, CH₃–CO–NH–CH₃) is a simple molecule that can be used to model a subset of the properties of polypeptides. The secondary amide functionality [R–C(O)–N(H)–R] present in NMA is ubiquitous in polypeptides as it constitutes the polymeric linkage that connects amino acids in these macromolecules. The equilibrium population of *trans*-NMA(aq) is roughly similar to that found in a polypeptide backbone where the *trans* arrangement of adjacent nonprolyl amino acids is favored by ~1000:1.¹ Thus, the solvent interactions driving the formation of the nonprolyl *cis*–*trans* conformers in polypeptides are reasonably approximated by NMA. For example, the transient binding of a water molecule to either the carbonyl oxygen, O*, or amide hydrogen, H*, in *trans*-NMA(aq) can be expected to reflect some important features of the aqueous solvation of a protein/polypeptide backbone. However, since NMA is a rather simple small molecule, it is amenable to study by high resolution/accuracy experimental and theoretical techniques that are not easily applicable to large systems.

The properties of NMA away from the *cis* and *trans* conformers are, also, of current interest. The twisting of *trans*-NMA about its nonprolyl peptide C(O)–N bond is a rare event that occurs much less frequently than the amino acyl-prolyl *cis*–*trans* isomerization process. (Note, for the latter the *cis*–*trans* population ratio is only about 4:1.¹) Indeed, nonprolyl isomer-

ization is a slow process that can be induced in proteins by its particular/unique sequence,² a nonprolyl isomerase,³ or an intermolecular binding event,⁴ which can in turn lead to the more efficient formation of secondary structural elements⁵ or, in contrast, hinder folding.^{6,7} Furthermore, the change in the C(O)–N bond order from a “partial-double” bond in either *trans*- or *cis*-NMA to a single bond near the transition state is typical of the electronic restructuring that occurs during either prolyl or nonprolyl isomerization in polypeptides and is still incompletely understood. For example, the definition of a “partial-double” bond in formamide remains the subject of debate.^{8,9} Consequently, it is desirable to study the “breaking” of this unusual bond.

In this article, finite-temperature simulation studies of NMA in vacuo and in water solvent are presented for both a CHARMM22 and a BLYP-DFT model description of the entire system (NMA + water). Both equilibrium simulations of the *trans* conformer as well as umbrella sampling computations along a preselected pathway to isomerization, the $\Omega = \angle \text{C}(\text{H}_3)\text{--C}(\text{O})\text{--N--C}(\text{H}_3)$ torsion angle, are given. This paper builds on our recent letter¹⁰ where the first ab initio^{11,12} description of the properties of fully solvated NMA(aq) were presented. Here, the computations are further mined in order to provide new insights. First, by comparing the solvation structure of NMA(aq) along the pathway to the structure of neat liquid water solvent at the same level of theory, the effect of the NMA solute on the water bonding network can be observed. Hydrogen bonds involving either O* or H* are characterized, providing a perspective on the solvation of the polypeptide and protein backbone hydrogen bonding groups. The thermodynamic, structural, and electronic properties of the NMA molecule itself, as it is twisted about the Ω angle, are explored as well. The geometric distortion of NMA and the accompanying electronic structure perturbations in the amide group recently revealed¹⁰

* Corresponding author. Present address: Computational Science, Department of Chemistry and Applied Biosciences, ETH Zurich, USI Campus, Via Giuseppe Buffi 13, CH-6900 Lugano, Switzerland. E-mail: ymantz@phys.chem.ethz.ch.

[†] IBM T.J. Watson Research Laboratory.

[‡] Université Pierre et Marie Curie.

[§] New York University.

^{||} Present address: Département de Chimie, Université de Montréal, Montréal H3C 3J7, Canada.

TABLE 1: Major Simulation Studies Performed (Symbols are Defined and Force Fields are Referenced in the Text)

force field	$N_{\text{H}_2\text{O}}$	L_{300} (Å)	\mathcal{T} (ns)	δt (fs)
NMA(g) about Ω				
BLYP		9.0/18.0 ^a	0.224 ^b	0.125
CHARMM22		15.0	4.480 ^c	6.0
NMA(aq) about Ω				
BLYP	27	9.687	0.224 ^b	0.125
CHARMM22	27	9.687	107.52 ^d	6.0
CHARMM22	232	19.105	4.480	6.0
eq-NMA(aq)				
BLYP	27	9.687	0.150	0.125
CHARMM22	27	9.687	3.000	6.0
CHARMM22	232	19.105	4.000	6.0

^a Specifies inner and outer box lengths. ^b Biased trans-NMA (bt-NMA): 0.056 ns; NMA near the barrier maximum (bts-NMA): 0.112 ns; biased cis-NMA (bc-NMA): 0.056 ns. ^c Performed $N_{\text{sim}} = 20$ times as long to estimate the BLYP error. ^d Only 4.480 ns are used to estimate the error in BLYP results.

using state-of-the-art analysis tools are discussed further, and the molecular dipole moment of NMA and the solvating water molecules during isomerization is calculated, allowing many-body polarization effects to be discerned. Both static (0 K) and thermodynamic energy profiles are presented, motivating a novel decomposition of the entropy change of reaction in terms of new thermodynamic quantities that can be physically interpreted at the molecular level.

The organization of the paper is as follows: In section II, the simulations details are given. In sections III–VI, the radial and angular solvent shell structures of NMA at selected points along a pathway to isomerization are analyzed. In section VII, the structural, energetic, and electronic properties of NMA during isomerization (and those of the neighboring water molecules) are discussed. Conclusions are drawn in section VIII.

II. Computational Models and Methods

Both ab initio and empirical MD sampling schemes as implemented in PINY_MD¹³ are employed to study *trans*-NMA-(aq) and the isomerization of NMA(g) and NMA(aq) along a preselected pathway, the $\Omega = \angle \text{C}(\text{H}_3)\text{--C}(\text{O})\text{--N--C}(\text{H}_3)$ torsion angle. Simulation details, including the number of H₂O molecules, $N_{\text{H}_2\text{O}}$, in the periodic cubic box of length L at temperature T , L_T , the data collection period, \mathcal{T} , and the simulation time step, δt , are given in Table 1. Results obtained from a given simulation are designated by labels such as “C22 eq-NMA + 232 H₂O” that are defined below. A discussion of the analysis of statistical uncertainty in configuration sampling is given in Appendix A, and more discussion of the MD methods and force fields is given below. In addition to the finite-temperature simulations described in the table, geometry optimizations of NMA(g) with constrained values of Ω are performed at the BLYP level of theory with a plane-wave basis set using PINY_MD¹³ and at the MP2 level of theory with a 6-311++G(d,p) basis set using Gaussian 98.¹⁴

The Car–Parrinello ab initio MD (AIMD) technique employed herein is an efficient combination of both MD and density-functional theory and thus permits the study of ground-state electronic structure and transient hydrogen-bond breaking and formation at finite temperature. The AIMD simulations are performed at the BLYP¹⁵ level of theory with a finite plane-wave (“pw”) basis set and are labeled AIMD (BLYP/pw) to emphasize the limitations of this technique. This choice of approximate functional is justified by the reasonable description of the water hydrogen bond reported in previous studies (see,

for example, ref 16) and is validated throughout by comparison to MP2 calculations. The basis set is truncated at $E_{\text{cut}} = 70$ Ry and a single k -point (Γ -point). Separate Nosé–Hoover chain thermostats¹⁷ for the ionic and electronic degrees of freedom are used for better temperature control. To improve adiabaticity, the hydrogen masses are set equal to that of oxygen, which preserves all static properties for classical nuclei. Nuclear quantum effects are neglected entirely in this work, introducing an additional error in the predicted solvent shell structure. Also, a preconditioning scheme is employed,¹⁸ such that the electronic fictitious “mass”, μ , is raised above 400 au for high-energy/frequency components of the plane wave expansion that might couple to the nuclei efficiently.

The CHARMM22¹⁹ (abbreviated C22) force field, which includes the TIP3P²⁰ H₂O model, is the empirical force field description selected for study in the present work. C22 is inexpensive to simulate and still widely used in large-scale biomolecular simulations. It captures the essence of many empirical models that are parametrized at a single state point. Such models often possess unphysically large energetic penalties for geometric distortions such as cis–trans isomerization.

Umbrella sampling MD and AIMD simulations of the torsional pathway to isomerization are performed in the usual way by introducing harmonic biasing potential terms centered at selected values of Ω , termed $\tilde{\Omega}_j$, to the force field. The potential of mean force is obtained from the biased data using the weighted histogram averaging method (WHAM), as reviewed in ref 21. In total, 28 runs are performed with different terms separated by 5° near the barrier regions in order to achieve sufficient sampling but by 15° elsewhere. Starting from an appropriate configuration (vide infra), each of the 28 AIMD (BLYP/pw) runs [of either BLYP NMA(g) or of BLYP NMA-(aq) in 27 BLYP H₂O molecules] is commenced by performing 1 ps (in vacuo) or 2 ps (in solution) of equilibration, followed by 8 ps of data collection for a total of 224 ps (Table 1). Three sets of 28 MD runs including C22 NMA(aq) in either 27 or 232 TIP3P H₂O molecules as well as C22 NMA(g) are also performed and run sufficiently long in order to obtain reasonably well-converged results. In this work, biased *trans*-NMA(aq), labeled “C22 bt-NMA + 27 H₂O”, is studied by analyzing 27 ns of data collected from seven different C22 runs with $\tilde{\Omega}_j$ values of $\pm 135^\circ$, $\pm 150^\circ$, $\pm 165^\circ$, and -180° ; biased *cis*-NMA, designated “C22 bc-NMA + 27 H₂O”, from seven C22 simulations with $\tilde{\Omega}_j$ values of 0° , $\pm 15^\circ$, $\pm 30^\circ$, and $\pm 45^\circ$; and biased “transition state” NMA, labeled “C22 bts-NMA + 27 H₂O”, from 54 ns of data collected from 14 runs with $\tilde{\Omega}_j$ values of $\pm 60^\circ$, $\pm 75^\circ$, $\pm 90^\circ$, $\pm 95^\circ$, $\pm 100^\circ$, $\pm 105^\circ$, $\pm 120^\circ$. One of the 28 C22 runs with $\tilde{\Omega}_j = -180^\circ$ is extended in order to obtain results for the solvent shell structure of C22 *trans*-NMA(aq) that are subsequently labeled “C22 eq-NMA + 27 H₂O” or “C22 eq-NMA + 232 H₂O”, respectively. On the other hand, results pertaining to “BLYP eq-NMA + 27 H₂O” are generated by extending five runs (with $\tilde{\Omega}_j$ values of -180° , $\pm 165^\circ$, and $\pm 150^\circ$) to improve the statistics.

An efficient dual length scale method²² is utilized to study the isomerization of NMA in vacuo under the DFT force field. A single NMA molecule is placed inside a small box of length 9 Å with a large plane-wave basis set cutoff of 70 Ry that is contained within an 18 Å simulation cell whose basis set cutoff is 10 Ry. The cluster boundary condition method of ref 23 is employed in the computations. This dual length scale scheme is several times more efficient than a conventional one and is just as accurate, i.e., isolated NMA in a 12 Å simulation cell

with a 70 Ry cutoff and employing the method of ref 23 to enforce cluster boundary conditions.

The umbrella sampling simulations of NMA(aq) along the isomerization pathway are set up as follows. First, two sets of 28 cells are obtained by “dunking” an NMA molecule whose geometry is optimized in vacuo under either the BLYP or C22 force field with a biasing potential centered at $\bar{\Omega}_j$ into an equilibrated box of TIP3P H₂O molecules. A third set of 28 cells is obtained by dunking only the C22-optimized NMA molecules into a larger TIP3P water box. In total, 84 simulation cells are generated, each of which contains a single NMA molecule in either 27 or 232 TIP3P H₂O molecules. Subsequently, each system is simulated for 200 ps in the NVT ensemble under C22, but with NMA held fixed, to equilibrate the surrounding H₂O's. Next, the 56 cells containing NMA molecules whose geometries were optimized using C22 are equilibrated with flexible NMA for 120 ps in the NPT ensemble under C22, followed by 200 ps of data collection to determine average box lengths $\bar{L} = 9.69$ Å (27 H₂O) or 19.11 Å (232 H₂O). The ratio of \bar{L} to a cell's length is used to translate the molecules and construct a new group of 84 simulation cells with a length of either 9.69 or 19.11 Å. Subsequently, these 84 cells are reequilibrated for 200 ps in the NVT ensemble, with NMA held fixed. The 28 cells containing NMA in a minimum geometry on the biased BLYP potential energy surface are used as initial configurations for umbrella sampling AIMD (BLYP/pw) in the NVT ensemble, i.e., 2 ps of equilibration is performed for every flexible BLYP NMA surrounded by 27 BLYP H₂O, followed by 8 ps of data collection. As for the remaining 56 cells, production runs are commenced with flexible C22 NMA surrounded by either 27 or 232 TIP3P H₂O in the NVT ensemble.

As an interesting aside, the molar volume of *eq*-NMA(aq) can be estimated from the C22 NPT simulations using $\bar{V}_{\text{NMA}} \approx \bar{L}^3 - 30 \cdot N_{\text{wtr}}$, where “30” is the molar volume in Å³ of a TIP3P H₂O molecule at 300 K. A range of \bar{V}_{NMA} values is calculated, 92–105 Å³, for NMA solvated by 27, 41, or 85 H₂O molecules. This corresponds to the volume of a sphere with 5.6–5.9 Å diameter that is only slightly greater than the maximum separation between hydrogen atoms on different methyl groups of the optimized *trans*-NMA(g) structure, i.e., 5.4 Å. The uncertainty in \bar{V}_{NMA} arises from taking the difference of two large numbers. The assumption of a single constant molar volume (of a TIP3P H₂O molecule) is more accurate as the box size is increased. However, the tradeoff is a greater uncertainty in \bar{L} that badly skews the final result, based on NPT simulations performed with up to 1000 H₂O molecules for 200 ps. Thus, a much longer NPT simulation with more than 85 H₂O molecules would be needed to obtain a better estimate.

III. Radial Distribution Functions of NMA in Liquid Water

To understand the hydrogen bonding interactions between water and NMA that are the dominant forces driving NMA solvation, appropriate radial distribution functions are examined, here. Of particular interest are the NMA amide hydrogen–water oxygen distribution, denoted $g_{\text{H}^*\text{O}}(r)$, and the NMA carbonyl oxygen–water hydrogen distribution, labeled $g_{\text{O}^*\text{H}}(r)$. First, however, an appropriate definition of the radial distribution function in concentrated solutions is given when a comparison to results generated at infinite dilution is desired. Subsequently, the distributions $g_{\text{H}^*\text{O}}(r)$ and $g_{\text{O}^*\text{H}}(r)$ predicted by the two different models, empirical and *ab initio*, are presented and discussed. Based on the two models' predictions of pure liquid

water structure, tentative conclusions are reached about the nature of the true $g_{\text{H}^*\text{O}}(r)$ and $g_{\text{O}^*\text{H}}(r)$ functions, which await the results of pending neutron diffraction experiments for confirmation. In addition, the two $g(r)$'s from points along the preselected reaction pathway, $\bar{\Omega}$, under C22 are shown. Minor differences between the solvent shell structures of *cis*, *trans*, and TS conformers of NMA(aq), where TS denotes the conformations at the top of the barrier of the selected pathway, are observed.

A definition of the radial distribution or pair correlation function for systems at finite concentration that enables comparison to systems at infinite dilution is required. In concentrated systems, e.g., BLYP NMA(aq) in 27 H₂O molecules, the finite volume of the solute is significant, and the solvent density in the simulation cell, ρ_{sln} , is different from that of the pure or neat bulk liquid, ρ_{slvt} . Therefore, it is useful to employ ρ_{slvt} as opposed to ρ_{sln} as the reference density in the definition of the radial distribution function. This is equivalent to scaling the standard definition by the ratio $\rho_{\text{sln}}/\rho_{\text{slvt}}$. In principle, this is a reasonable approach, but it should be noted that at large distances the distribution function will no longer converge to unity but rather to $\rho_{\text{sln}}/\rho_{\text{slvt}}$. However, the interest lies in short and intermediate range order where an inappropriate choice of reference density, ρ_{sln} , will distort comparisons. In contrast, the running coordination number, $n(r)$, is invariant to the choice of reference density.

To place the NMA–water distribution functions defined above into the proper context, a comparison is made with the corresponding water–water distribution functions. The first (intermolecular) peak of the C22 $g_{\text{O}^*\text{H}}(r)$ is shifted to a slightly smaller distance, r , compared to the analogous feature in the $g_{\text{OH}}(r)$ of neat liquid TIP3P water (Figure 1, top panel). This shift is not surprising, given the larger dipole moment of the C=O group in C22 NMA(aq), 3.01 D, compared to that of a rigid TIP3P H₂O molecule, 2.35 D. The implication is that the hydrogen bond formed between the carbonyl oxygen and the water hydrogen is stronger than water oxygen–water hydrogen bond interaction (i.e., water would prefer to donate hydrogen bonds to NMA under C22). However, the strength of a hydrogen bond is a complex function of several degrees of freedom,²⁴ and a calculation of the potential energy surface would be required to confirm this hypothesis. Interestingly, this small shift of the first (intermolecular) peak is not reproduced by AIMD (BLYP/pw). A longer simulation of BLYP NMA(aq) that is also approaching the basis set limit (e.g., 150 Ry) might reveal a change that is more consistent with the empirical model prediction, although this is unlikely. On the other hand, both models unambiguously predict a substantial shift of the first (intermolecular) peak of $g_{\text{H}^*\text{O}}(r)$ to larger values of r (Figure 2, top panel), which is rationalized by the smaller dipole moment of the N–H group, e.g., 1.89 D in C22 NMA(aq), leading to weaker electrostatic interactions. As described in ref 25, these observations are consistent with a comparison between gas-phase quantum-chemical computations on the water dimer and the NMA–water dimer.^{26–28}

Some statistically significant differences are observed between the AIMD (BLYP/pw) and C22 NMA–water radial distribution functions. First, the smallest values of r for which these functions are nonzero are markedly different. In fact, this discrepancy is similar to that observed between AIMD (BLYP/pw) and TIP3P water¹⁶ and is attributed primarily to the parametrization of C22. In addition, an overstructuring, of $g_{\text{H}^*\text{O}}(r)$ in particular, is predicted by AIMD (BLYP/pw) relative to C22. This effect lies outside of the calculated error bars, $\sigma(r)$, in the middle panels

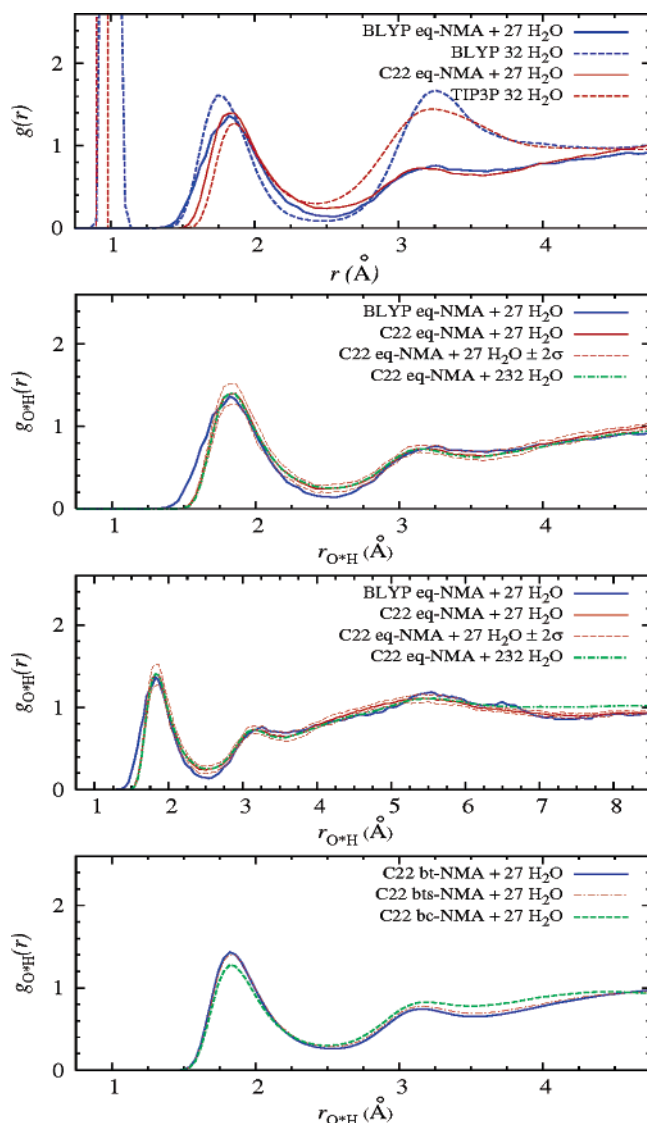


Figure 1. (Top panel) Predicted $g_{O^*H}(r)$ values between the NMA-(aq) carbonyl oxygen, O^* , and the water hydrogens, as well as the $g_{OH}(r)$ values for pure liquid water,¹⁶ under both BLYP and C22. (Middle panels) Error analysis of the BLYP $g_{O^*H}(r)$ employing C22 eq-NMA(aq) plotted over two different axis ranges. (Bottom panel) C22 $g_{O^*H}(r)$ values along Ω (0.04 Å bin).

of Figures 1 and 2 (see Appendix A). At distances of 4–5 Å or less, finite-size effects are insignificant, based on the near-perfect overlap of the $g(r)$'s obtained for C22 eq-NMA(aq) in 27 versus 232 H_2O molecules (Figures 1 and 2), whose functions are in reasonable agreement with those obtained elsewhere,²⁹ using a different (empirical) force field. Because the first peaks of the oxygen–oxygen and oxygen–hydrogen distribution functions for pure liquid water are reasonably reproduced by BLYP,¹⁶ while the first peak of the TIP3P model is understructured, it is possible that the BLYP result more closely approximates the true result. However, the number of water molecules in the first solvation shell of eq-NMA(aq) predicted by both models is similar, roughly two surrounding the carbonyl oxygen and one around the amide hydrogen, despite the significant differences in the predicted $g(r)$'s, indicating that the two models are both capturing the essential physics of the interaction.

Next, the changes in the NMA–water hydrogen bonding distribution functions along the torsional reaction coordinate are discussed. As *trans*-NMA(aq) is twisted about Ω , the solvent shell structure is basically unaffected until *cis*-NMA(aq) is

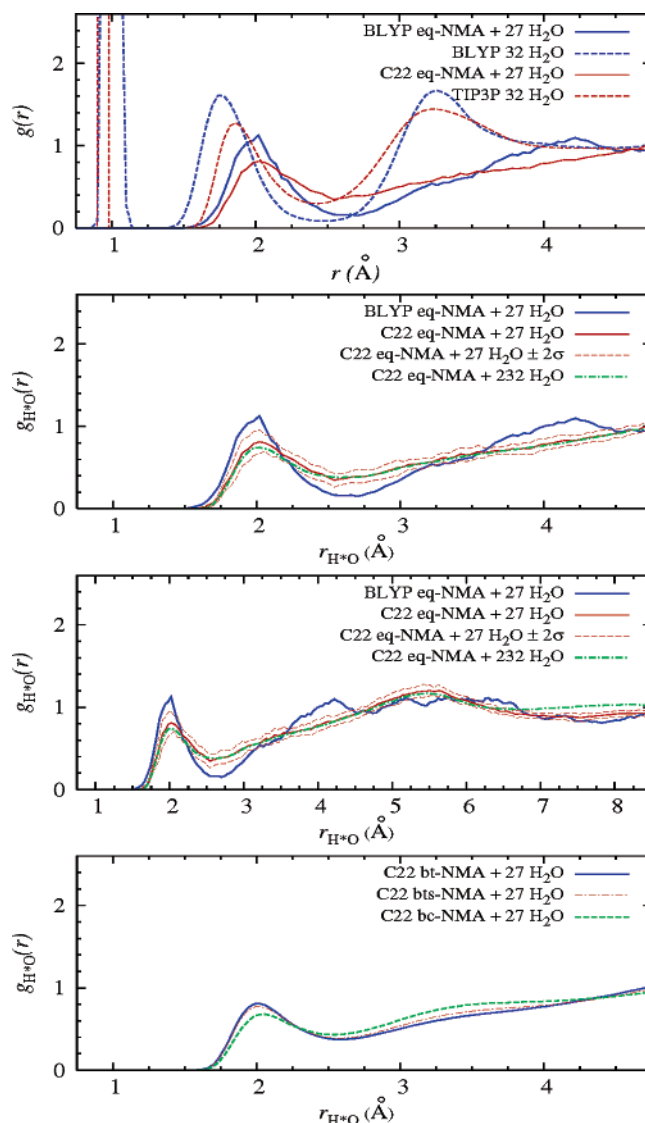


Figure 2. (Top panel) Predicted $g_{H^*O}(r)$ values between the NMA-(aq) amide hydrogen, H^* , and the water oxygens, as well as the $g_{OH}(r)$ values for pure liquid water,¹⁶ under both BLYP and C22. (Middle panels) Error analysis of the BLYP $g_{H^*O}(r)$ employing C22 eq-NMA(aq) plotted over two different axis ranges. (Bottom panel) C22 $g_{H^*O}(r)$ values along Ω (0.04 Å bin).

approached. That is, both $g_{O^*H}(r)$ and $g_{H^*O}(r)$ describing C22 bc-NMA(aq) are slightly less structured than those of either bt-NMA(aq) or the “transition state” predicted by the approximate/proposed reaction coordinate (bottom panel of Figures 1 and 2). However, the number of water molecules in the first solvation shell is reduced by only 0.1 H_2O molecule. These relatively minor changes might be explained by the syn position of both methyl groups in *cis*-NMA(aq), causing the H_2O molecules interacting with O^* and H^* to interfere with each other (see Section VI). No statistically significant trend is predicted by AIMD (BLYP/pw).

IV. Spatial Map of Water Molecules Surrounding C22 NMA

To understand the packing of H_2O molecules surrounding NMA(aq), it is useful to construct the three-dimensional spatial maps of water hydrogen atoms and water oxygen atoms about the NMA molecule. This is a highly intuitive tool that reveals both the radial and angular solvation shell structure,^{16,30} the latter of which is averaged out in the radial distribution function, $g(r)$.

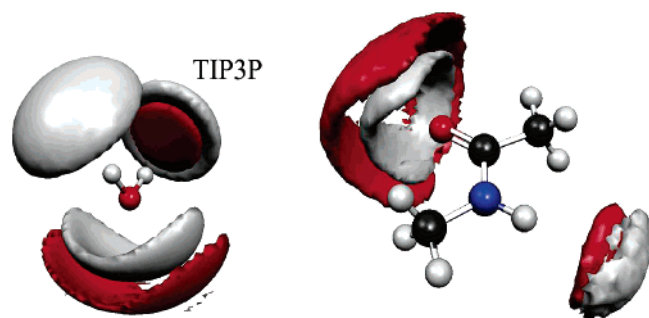


Figure 3. The first solvation shell of TIP3P water at 300 K and that surrounding C22 *eq*-NMA(aq) in 232 H₂O molecules. The enclosed (red or gray) isosurface regions depicted for $r \leq 4.2$ Å have average oxygen or hydrogen densities at least 3.5 or 1.75 times greater, respectively, than that of the bulk. Equivalently, the isosurface values are $P_O(r) = 3.5$, $P_H(r) = 1.75$.

The spatial maps are defined such that

$$g_{YX}(r;T)4\pi r^2 = \int_{D(V)} P_X(\mathbf{r};T) \delta(\mathbf{r} - r) d\mathbf{r}$$

$$\rho_X \int_{D(V)} P_X(\mathbf{r};T) d\mathbf{r} = N - 1 \quad (1)$$

where Y is either O, O*, or H*, while X = H or O of the surrounding H₂O's. Far from the NMA molecule, the spatial maps approach the uniform density limit, $\lim_{|\mathbf{r}| \rightarrow \infty} P_X(\mathbf{r};T) \rightarrow 1$. The spatial map of the first solvation shell structure of C22 *eq*-NMA(aq) in 232 H₂O molecules simulated for $\mathcal{T} = 4.0$ ns of data collection is compared to the spatial map of TIP3P liquid water, below. The maps from the other simulations performed for less than 4.0 ns of data collection are not fully converged.

In Figure 3, the red (oxygen) and the gray (hydrogen) lobes depict regions where H₂O molecules are likely to be found in the local frame of the central H₂O or NMA molecule. The fairly uniform spatial arrangement of water molecules in the first solvation shell surrounding the carbonyl oxygen atom, O*, in C22 *eq*-NMA(aq) is consistent with the distribution of neighbors in TIP3P liquid water (Figure 3). Thus, the single red cupped lobe representing the donating water molecules' oxygen atoms in TIP3P water is replaced by two bands joined at their ends surrounding O* in C22 *eq*-NMA(aq). The "hole" in the center is due to steric interference between the (on average, two) donating H₂O molecules. Both features, the cup in liquid water and the bands around O*, are highly delocalized due to the absence of lone pair charges on the oxygen atoms. Thus, a more localized distribution surrounding O* is anticipated for BLYP *eq*-NMA(aq). Additional support for this prediction is provided by the calculated electron localization functional presented later in the text for selected configurations of NMA(aq) as it is twisted about the Ω torsion angle. The description of the electron lone pairs at O* is similar to that observed on the oxygen atoms in liquid water.³¹

The spatial regions describing hydrogen bond acceptor H₂O molecules in liquid water and in NMA(aq) are similar. In TIP3P water, the regions or "caps" in the upper hemisphere of the local frame are nearly identical due to the strong directionality of hydrogen bonding imposed by the donating hydrogen atoms of the central H₂O molecule. Examining the analogous spatial map of C22 NMA(aq), a single (on average) H₂O neighbor is in contact with the amide hydrogen, H*. The spatial extent of the caps is slightly less than that observed in liquid water, due to the fact that the amide hydrogen-water oxygen hydrogen bond is weaker and, thus, more easily broken as described above.

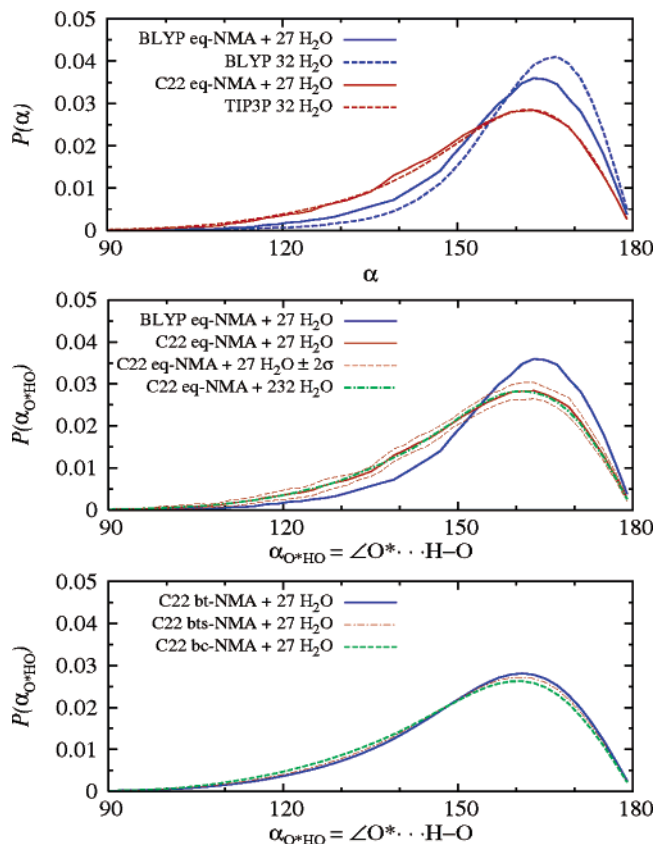


Figure 4. (Top panel) Predicted $P(\alpha_{O^*HO})$ values between the NMA-(aq) carbonyl oxygen, O*, and the water hydrogens, as well as the $P(\alpha_{OHO})$ values for pure liquid water,¹⁶ under both BLYP and C22. (Middle panel) Error analysis of the BLYP $P(\alpha_{O^*HO})$ employing C22 *eq*-NMA(aq). (Bottom panel) C22 $P(\alpha_{O^*HO})$ values along Ω (2° bin).

V. Hydrogen-Bond Angular Distributions of NMA in Liquid Water

The probability density of hydrogen bond angles formed between NMA(aq) and the neighboring H₂O molecules provides complementary information to the radial distribution function. The distribution of two important angles, $\alpha_{O^*HO} = \angle O^*A \cdots H_D - O_D$ (Figure 4) and $\theta_{H^*OH} = \angle H^*D \cdots O_A - H_A$ (Figure 5), predicted by AIMD (BLYP/pw) and C22 are compared here. These distributions are obtained by averaging over all donating and accepting H₂O molecules interacting with O* and H*, respectively, in the first solvation shell taken as the first (intermolecular) minimum of the appropriate radial distribution function, i.e., either $g_{O^*H}(r)$ or $g_{H^*O}(r)$. The principle conclusion is that those of C22 are understructured, consistent with its predictions for the (analogous) distributions in pure liquid water.¹⁶ The BLYP distributions may be approximately correct, as BLYP does a reasonable job predicting the first solvation shell of the neat solvent,¹⁶ although this is by no means a guarantee. Both $P(\alpha_{O^*HO})$ and $P(\theta_{H^*OH})$ are examined along the preselected reaction pathway, Ω , indicating slightly different hydrogen bond angles in *cis*- versus *trans*-NMA(aq).

The geometry of the O*—H and H*—O hydrogen bonds compared to those in liquid water predicted by both methods in section III are consistent with the calculated angular distributions presented here (Figures 4 and 5). The C22 NMA(aq) and TIP3P H₂O distributions of α_{O^*HO} and α_{OHO} , respectively, are essentially identical (Figure 4), indicating that $P(\alpha_{O^*HO})$ is unaffected by the slightly shorter O*—H hydrogen bond relative to the O—H hydrogen bond in TIP3P liquid water (Figure 1). On the other hand, the BLYP NMA(aq) distribution of α_{O^*HO}

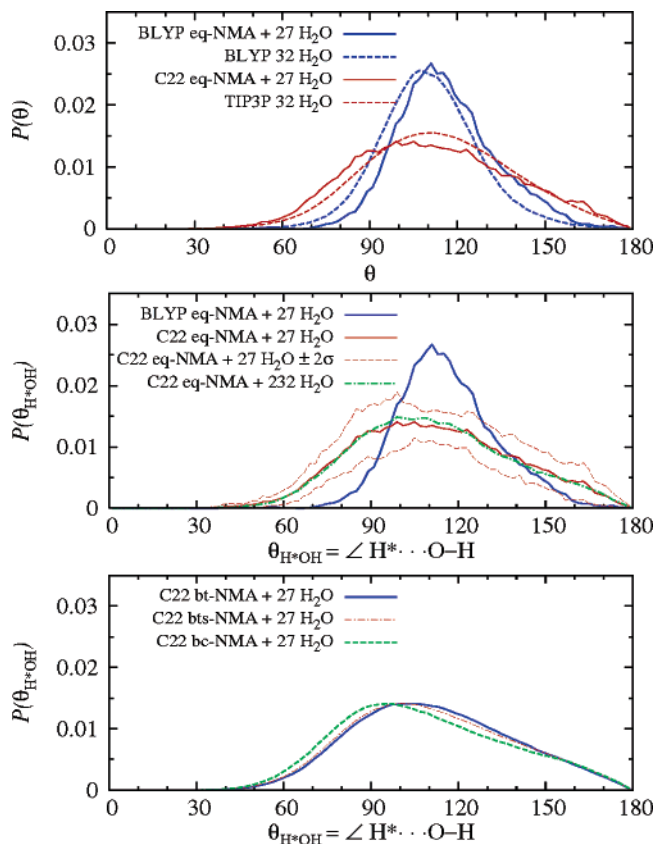


Figure 5. (Top panel) Predicted $P(\theta_{\text{H}^*\text{OH}})$ values between the NMA-(aq) amide hydrogen, H^* , and the water oxygens, as well as the $P(\theta_{\text{HOH}})$ values for pure liquid water,¹⁶ under both BLYP and C22. (Middle panel) Error analysis of the BLYP $P(\theta_{\text{H}^*\text{OH}})$ employing C22 eq-NMA-(aq). (Bottom panel) C22 $P(\theta_{\text{H}^*\text{OH}})$ values along Ω (2° bin).

is slightly flattened and shifted to smaller values of α compared to $P(\alpha_{\text{OH}_2})$ in BLYP water, consistent with the prediction of a longer O^*-H hydrogen bond. Both methods are predicting a discernible shift of $P(\theta_{\text{H}^*\text{OH}})$, but in opposite directions, relative to the distributions of θ_{HOH} in pure liquid water (Figure 5).

The NMA(aq) angular distributions predicted by AIMD (BLYP/pw) are markedly different from those obtained under C22. In particular, both the BLYP $P(\alpha_{\text{O}^*\text{HO}})$ and $P(\theta_{\text{H}^*\text{OH}})$ are sharper than those of the C22 model. This enhancement is significant and not a finite-size effect, based on the calculated, angle-dependent error bars depicting the uncertainty in the BLYP results and comparison between the distributions of C22 eq-NMA(aq) in 27 versus 232 H_2O molecules, as shown in Figures 4 and 5, middle panels.

The minor differences in the solvation shell structure of *cis*-NMA(aq) compared to that at other points along the preselected reaction pathway, Ω , revealed in section III are, also, observed here. The slightly flattened C22 *cis*-NMA(aq) $g(r)$'s, implying less structure, are consistent with the very slight (i.e., barely significant) broadening in both $P(\alpha_{\text{O}^*\text{HO}})$ and $P(\theta_{\text{H}^*\text{OH}})$ that is observed for C22 *cis*-NMA(aq) relative to other conformers (Figures 4 and 5).

VI. Beyond “Traditional” Measures of the Solvent Shell: Joint Probability Density Functions

In this section, the radial and orientational order of the water molecules surrounding NMA is characterized using joint radial and angular distribution functions.^{16,32} After describing the functions themselves, the solvation shell structures of BLYP and C22 NMA(aq) are examined in detail. The solvent structure

around C22 NMA(aq) in 232 TIP3P H_2O molecules is examined first, because the calculated functions include both the short- and long-range correlations of interest. At the same time, these functions are somewhat less structured compared to those of BLYP and comparatively simple to interpret. Next, a comparison is made between C22 predictions along the preselected reaction coordinate connecting the *cis* and *trans* isomers, and the section concludes with a discussion of the functions predicted by the BLYP model of NMA(aq).

It is useful to define two 3D distribution functions with two independent variables, a distance and a common angle, in order to characterize the interaction of NMA with a nearby H_2O molecule. The first function, $g_2(r_{\text{O}^*\text{H}}, \cos \alpha_{\text{O}^*\text{HO}})$, is defined by the radial distance between the carbonyl oxygen, O^* , and the hydrogen atom, H , of a (not necessarily neighboring) H_2O molecule and the cosine of the $\angle \text{O}^*\text{HO}$ angle formed by the O^*-H intermolecular distance and the $\text{H}-\text{O}$ intramolecular bond of the H_2O molecule. The second quantity, $g_2(r_{\text{H}^*\text{O}}, \cos \theta_{\text{H}^*\text{OH}})$, is defined similarly but with respect to the amide hydrogen, H^* , and the oxygen atom, O , of a (not necessarily neighboring) H_2O molecule. In either case, the standard radial distribution function is recovered by integration:

$$g(r; T) = \frac{1}{2} \int_{-1}^1 g_2(r, \cos \theta; T) d(\cos \theta) \quad (2)$$

Note that $g_2(r, \cos \theta; T)$ approaches unity at large radial distance, thereby justifying the choice of $\cos \theta$ as an independent variable.

The structural correlations through the third solvation “shell” of *trans*-NMA(aq) are revealed by an analysis of the $g_2(r_{\text{O}^*\text{H}}, \cos \alpha_{\text{O}^*\text{HO}})$ function predicted for C22 eq-NMA(aq) in 232 TIP3P H_2O molecules. The distribution given in Figure 6 exhibits several distinct maxima. The first, at (1.82 Å, −1), is an intense (white) peak surrounded by a high density of contour lines arising exclusively from the water hydrogen atoms that are participating in hydrogen bonds with the O^* atom, while that at (3.1 Å, 0.5) is assigned to the other hydrogen atom of the hydrogen-bonded H_2O molecules that is *not* interacting with O^* . Thus, both of these peaks originate from H_2O molecules in the first solvation shell surrounding O^* . The peak at (4.46 Å, −1) is due to the nearest hydrogen atom of H_2O molecules in the second solvation shell, that is, H_2O molecules interacting with the H_2O molecules hydrogen bonded to O^* , as illustrated in Figure 7. The maximum at (5.1 Å, 0.075) is primarily attributed to the other, more distant hydrogen atom of the H_2O molecules in the second solvation shell (Figure 7). (The steep ridge characterizing this peak at $r_{\text{O}^*\text{H}} \approx 5$ Å arises from a likely energetically unfavorable distortion of the hydrogen bond connecting the second shell molecules to the first shell.) In addition, third solvation shell molecules that are nearby also are contributing (Figure 7), resulting in a slanted, oval-shaped maximum. The elongated feature peaked at (6.54 Å, 1) arises from the other hydrogen atoms of H_2O molecules that are relatively near to O^* in the third solvation shell, while the weak feature at (7.18 Å, −1) is attributed to H_2O molecules in the third solvation shell that are further away from the O^* atom, i.e., connected to O^* through a linear, as opposed to bent, chain of hydrogen bonds (Figure 7).

Despite the dramatic changes in the contour plots themselves, the physical changes in the solvation shell structure along the reaction coordinate are comparatively minor. The contours plots of NMA(aq) in 27 H_2O molecules are shown in Figure 6 and are drawn over a reduced x -axis range, $r_{\text{O}^*\text{H}} \leq 4.75$ Å. Over this range, the map of C22 *bt*-NMA(aq) is virtually identical to that of C22 eq-NMA(aq) in 232 H_2O molecules, described

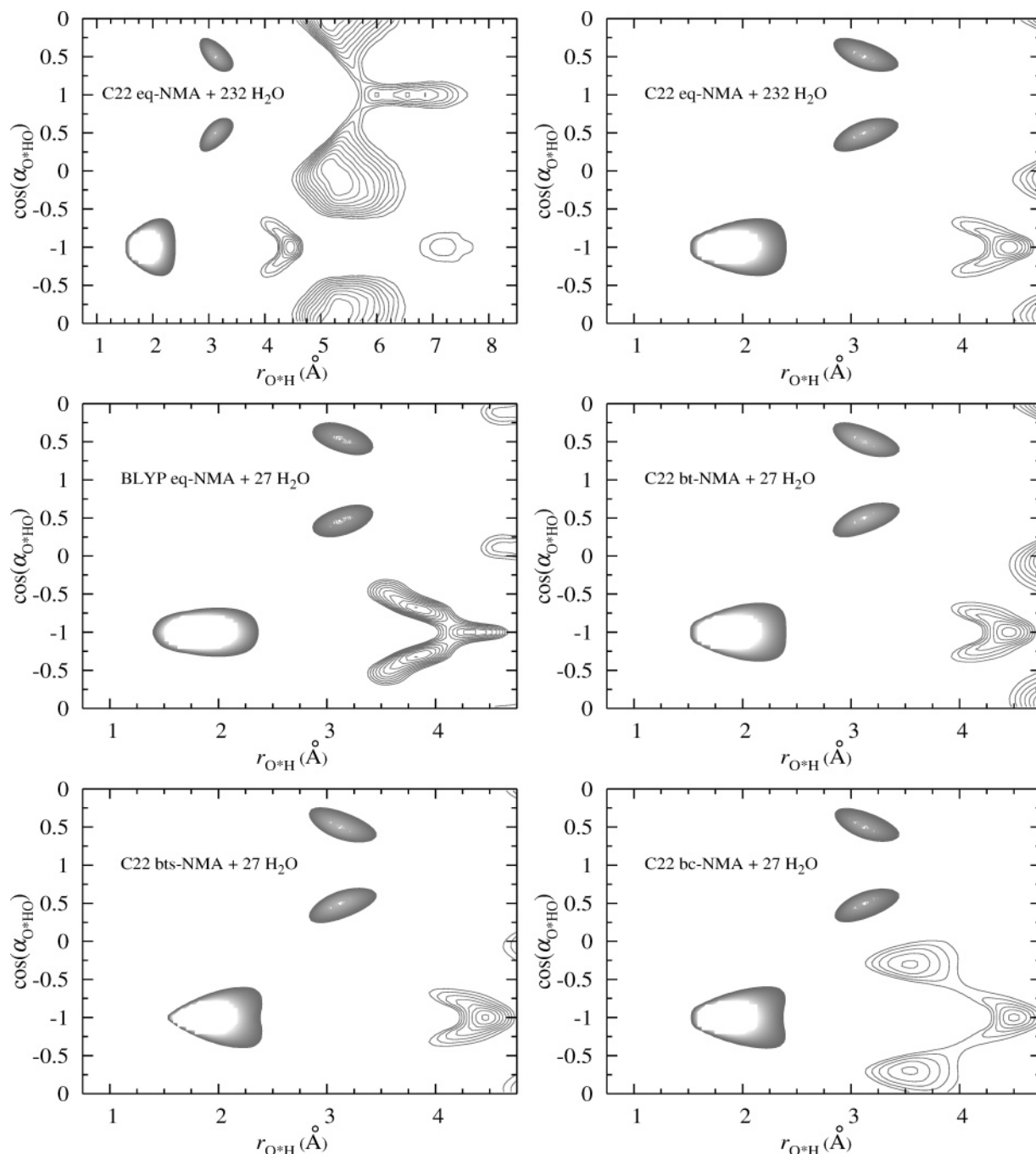


Figure 6. Predicted $g_2(r_{O^*H}, \cos \alpha_{O^*H_O})$ contour maps of C22 *eq*-NMA(aq) over two different axis ranges, BLYP *eq*-NMA(aq), and C22 *bt*-NMA(aq), *bts*-NMA(aq), and *bc*-NMA(aq). Only contour lines equal to or greater than 1.05 are shown, and the spacing is 0.025.

above. In addition, the contour plot of C22 *bts*-NMA(aq) is quite similar to that of C22 *bt*-NMA(aq). On the other hand, the most obvious difference between C22 *bt*-NMA(aq) and *bc*-NMA(aq) is the presence of an additional maximum in the contour plot of *bc*-NMA(aq) at (3.54 Å, -0.325) and the “disappearance” of solvation shell structure at larger values of r_{O^*H} . These effects are at least partially due to the formation of “ring” structures made possible by the *cis* position of the methyl groups and include some H₂O molecules that are bonded to either the O* or H* atom of NMA(aq) (Figure 8).

The difference in the solvation shell structure between the BLYP and C22 models of *eq*-NMA(aq) (Figure 6) can be rationalized by a more structured second solvation shell induced by the BLYP functional. In particular, note the presence of an additional maximum at (3.82 Å, -0.675) and an inward shift of the other nearby maximum to (4.30 Å, -1). Under C22 *eq*-

NMA(aq), this feature is due to H₂O molecules in the second solvation shell surrounding O*.

Further insight is gained by an analysis of the $g_2(r_{H^*O}, \cos \alpha_{H^*O})$ distribution function determined for C22 *eq*-NMA(aq) in 232 TIP3P H₂O molecules (Figure 9). The global maximum at (2.02 Å, -0.375) is due to the oxygen atoms of the H₂O molecules hydrogen bonded to H*. Three other maxima are located over a range of values of $r_{H^*O} \approx 5.5$ Å. The peak at (5.62 Å, 1) is likely due to the (H)O—H group of a first shell H₂O molecule that is hydrogen bonded to O* (Figure 10). The other two features could be assigned to the hydrogen atom *not* interacting with O* of the H₂O molecule hydrogen bonded to this atom. However, the latter assignment is problematic; these three peaks, which have different r_{H^*O} values, are assigned to the same H₂O molecule and thus are expected to have identical values of r_{H^*O} . In any event, conspicuously absent are features

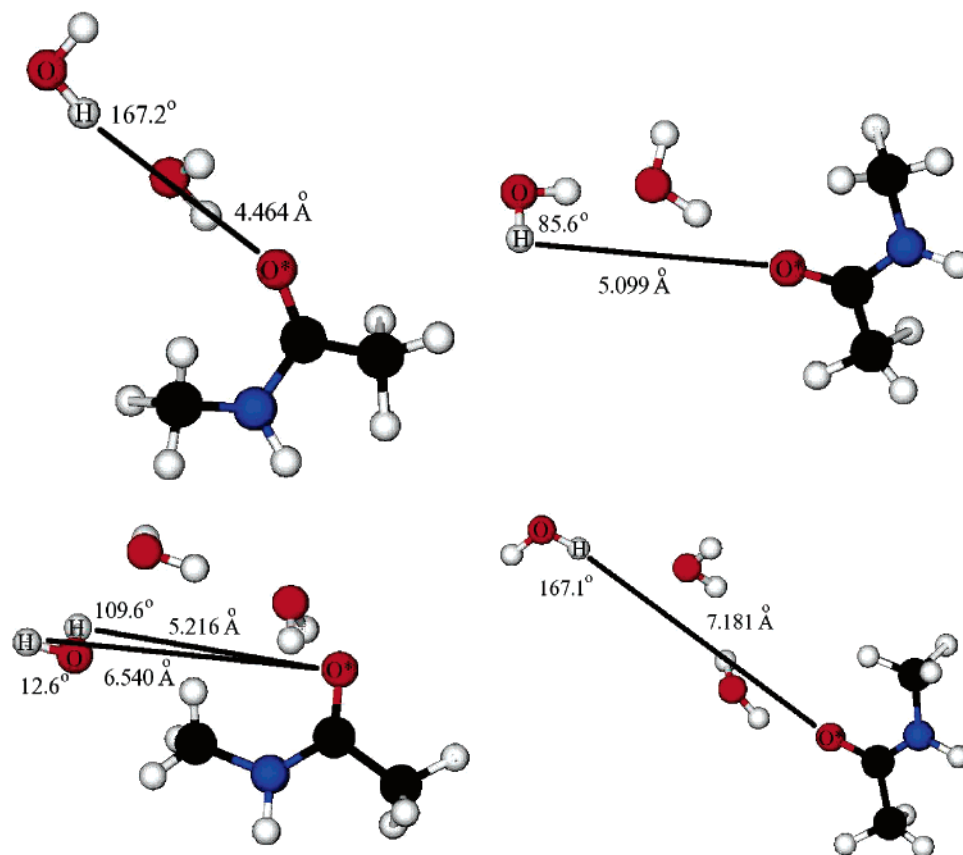


Figure 7. Selected molecules involved in the solvation of C22 eq-NMA(aq) in 232 H₂O molecules.

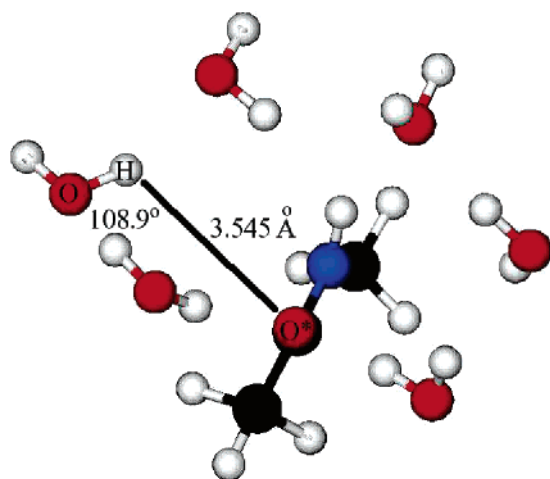


Figure 8. Selected molecules involved in the solvation of C22 *bc*-NMA(aq) in 27 H₂O molecules.

that would be expected from H₂O molecules in the second solvation shell of H* between about $3.0 \text{ \AA} < r_{\text{H}^*\text{O}} < 4.1 \text{ \AA}$. In the correct assignment, the single H₂O molecule bonded to H* is able to rotate about its hydrogen bond (to H*), resulting in a random orientation of this H₂O's hydrogen atoms and of the molecules in the second solvation shell surrounding H*. This results in the absence of structure over the range of values shown. (Also for this reason, no structural features in the contour plot of $g_2(r_{\text{O}^*\text{H}}, \cos \alpha_{\text{O}^*\text{H}\text{O}})$ are attributed to H₂O molecules surrounding H*.) Interestingly, however, the more structured BLYP eq-NMA(aq) contour map exhibits two maxima at $(4.10 \text{ \AA}, -0.475)$ and $(4.18 \text{ \AA}, 0.175)$ (Figure 9) that, if statistically significant, suggest the formation of a quasi-rigid arrangement of neighbors around the H₂O molecule hydrogen bonded to H*, preventing its free rotation. As C22 NMA(aq) is twisted about

its C(O)–N bond, the position of the single global maximum shown changes slightly from 112° (*bt*-NMA) to 106° (*bts*-NMA) to 103° (*bc*-NMA), while the peak itself is reduced in height by 20% (Figure 9), an effect that is averaged out in the calculation of the 2D angular distributions (section V) (i.e., an average over a range of radial distances is performed.)

VII. Properties of NMA and Solvent During Isomerization

The properties of NMA and water solvent along the preselected reaction pathway, the $\Omega = \angle \text{C}(\text{H}_3)\text{--C}(\text{O})\text{--N--C}(\text{H}_3)$ torsion angle, are discussed in detail. First, the choice of reaction coordinate is justified. Subsequently, the energetic changes during isomerization are presented, permitting a calculation of the entropy change, which is analyzed in a novel way that motivates an analysis of structural changes in the NMA molecule as a function of Ω . The dramatic distortion of bond lengths and angles observed near the barrier maximum is due to electronic structure changes in the amide group, specifically, a reduction in the C(O)–N bond order and C \rightarrow N atomic charge transfer, described in ref 10 and discussed further here. In addition, the molecular dipole moment of the surrounding solvent molecules is characterized, revealing an increase of this quantity for H₂O molecules interacting with the carbonyl oxygen, O*, of NMA(aq).

Although the true reaction pathway is a complex function of several degrees of freedom, the additional degrees of freedom that might couple to Ω have relatively small energetic barriers. First, the twisting of NMA about Ω is accompanied by a “flipping” of the amide hydrogen, H*, from a (roughly) antiparallel to parallel position relative to O*,^{33,34} or a change in the value of the angle $\angle \text{C}(\text{H}_3)\text{--C}(\text{O})\text{--N}(\text{H})\text{--H}$, from 0° to 180° . Besides this “flipping”, two additional degrees of freedom

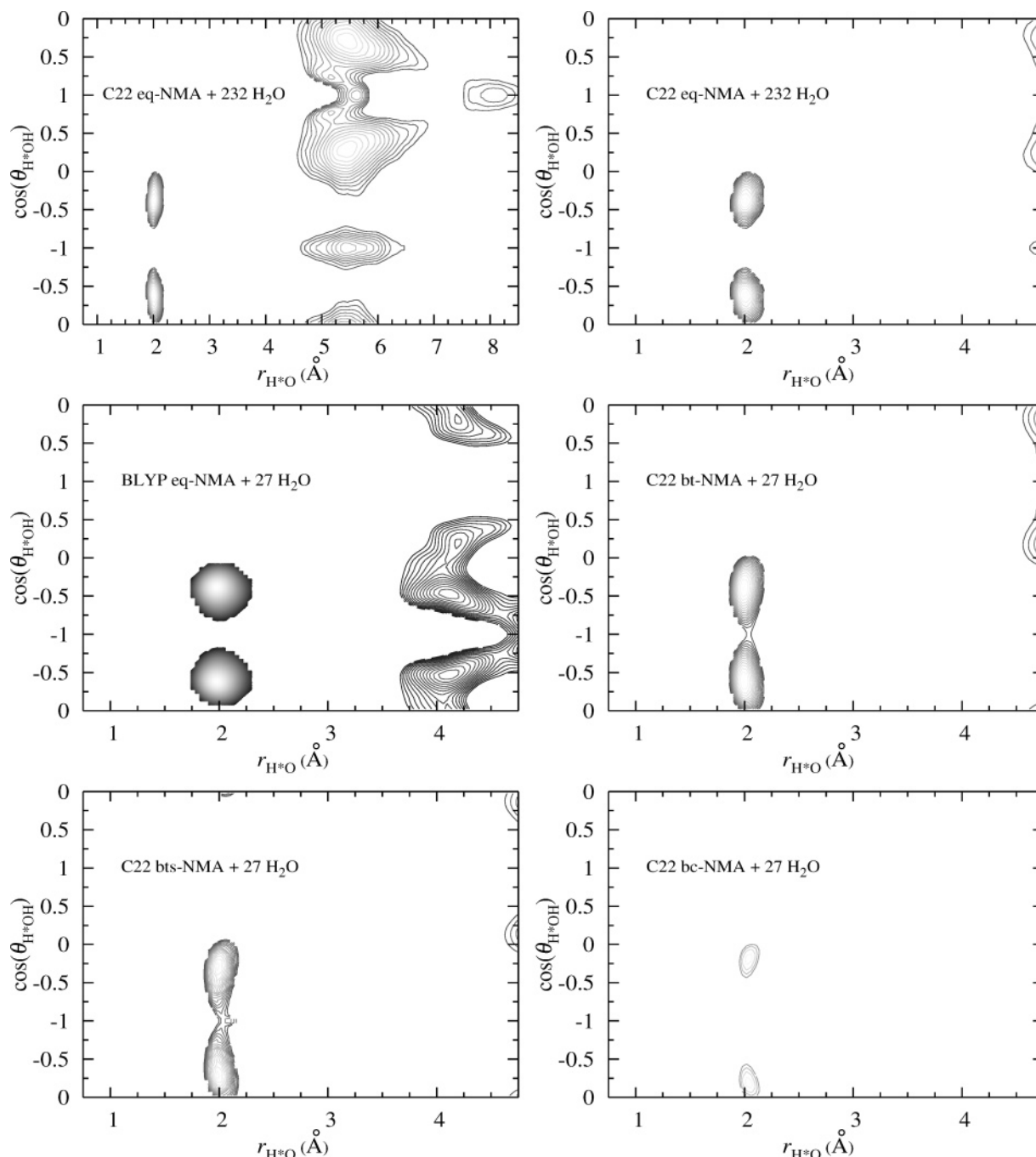


Figure 9. Predicted $g_2(r_{H^*O}, \cos \theta_{H^*OH})$ contour maps of C22 eq-NMA(aq) over two different axis ranges, BLYP eq-NMA(aq), and C22 bt-NMA(aq), bts-NMA(aq), and bc-NMA(aq). Only contour lines equal to or greater than 1.05 are shown and are incremented by 0.025.

are the rotation of the methyl groups, generating four local minima in the potential energy surface characterized by specific values of the angles ϕ and ψ .^{35,36} However, the energies associated with these additional motions are relatively small. Specifically, the free energy barrier surmounted by the “floppy” amide hydrogen is only 1.3 kcal/mol, which is estimated by performing a long MD simulation of C22 NMA(g) with a constrained value of Ω , 97° , and unbiasing the resultant probability distribution function.²¹ Furthermore, the energy difference between methyl rotamers in *trans*-NMA(g) is only 0.41 kcal/mol (BLYP/70 Ry), 0.38 kcal/mol (BLYP/110 Ry), or 0.76 kcal/mol (C22), whereas the values in *cis*-NMA(g) are 1.03, 1.09, and 2.96 kcal/mol, respectively. Thus, at $T = 300$ K, only $\approx 2 kT$ is needed to sample fully these additional degrees of freedom in BLYP NMA(g), and a more expensive calculation including a multidimensional reaction coordinate is not war-

ranted. On the other hand, solvent degrees of freedom might be expected to play a significant role in solution. However, the preceding analysis of C22 solvation structures along the reaction path indicates that the distribution of solvent molecules does not change dramatically. Thus, a one-dimensional coordinate can be taken to model approximately the isomerization process in solution.

A. Thermodynamic Changes during Isomerization. The static (0 K) relative energy, ΔE_o , profiles of NMA(g), obtained by optimizing structures with constrained values of Ω at different levels of theory, have interesting shapes (Figure 11). The curves calculated under C22, at the BLYP level of theory with a planewave basis set, and at the MP2 level of theory with a (localized) 6-311++G(d,p) basis set are in excellent agreement with each other and other method/basis set combinations^{37,38} at points near *trans*- and *cis*-NMA(g). In fact, $\Omega = 174^\circ$ is more

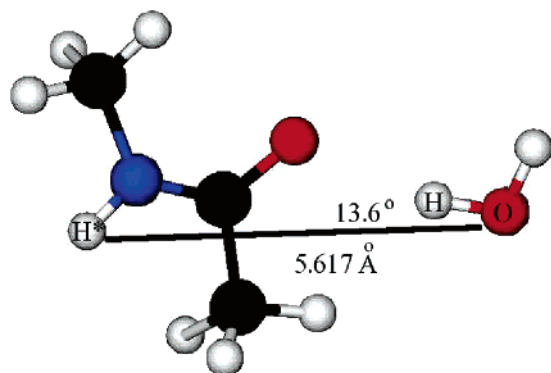


Figure 10. A selected molecule involved in the solvation of C22 eq-NMA(aq) in 232 H₂O molecules.

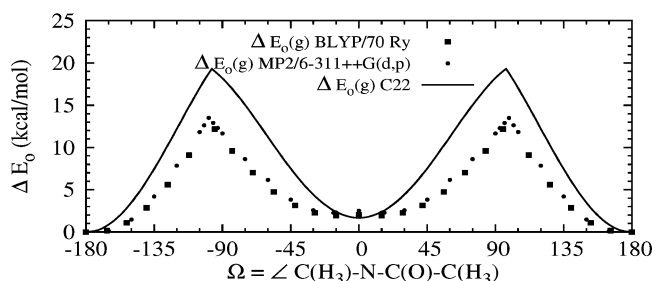


Figure 11. Static (0 K) NMA(g) energy profiles not including a zero-point energy correction.

stable (by 0.05 kcal/mol) than $\Omega = 180^\circ$ at the MP2/6-311++G(d,p) level of theory, while under both of the latter two methods, $\Omega \approx 15^\circ$ is more stable than $\Omega = 0^\circ$, in agreement with others.³⁸ (For further discussion, see ref 39.) However, the C22 model curve is generally “steeper” due to improper dihedral terms in the potential function.¹⁹ More importantly, the C22 prediction is substantially different, by several kcal/mol, from the other methods near the barrier maximum. Note that the predicted barrier height from the MP2/6-311++G(d,p) calculations performed here, 13.5 kcal/mol, is somewhat different from an earlier value,³⁴ 16.8 kcal/mol, which is the relative energy

(of the relevant stationary point) obtained at the MP2 level of theory with a 6-31G(d) basis set, indicating a basis set effect.

The relative Helmholtz free energies, ΔA , extracted from the umbrella sampling simulations of BLYP and C22 NMA(g) and NMA(aq),¹⁰ also exhibit some significant differences (Figure 12). The ΔA 's of BLYP and C22 *cis*-NMA(g) are similar, but those obtained for *cis*-NMA(aq) are in disagreement, which is explained by the calculated dipole moments. In the AIMD (BLYP/pw) simulations, the dipole moment of *cis*-NMA is larger than that of *trans*-NMA (in either gas or aqueous phases), and thus *cis*-NMA(aq) is stabilized by dipolar coupling with polar water molecules to a greater extent than *trans*-NMA(aq). However, the dipole moment of C22 *trans*-NMA is slightly larger than that of *cis*-NMA, leading to a destabilization of *cis*-NMA(aq) relative to *trans*-NMA(aq). Regardless of model, the solvation free energy for both *cis*- and *trans*-NMA(aq) is roughly the same, which is in agreement with both experimental and theoretical model predictions.⁴⁰ Another difference is that the BLYP model predicts a significantly lower barrier height, in both gas and aqueous phases. The uncertainty in the AIMD (BLYP/pw) ΔA profiles is $\pm 2\sigma(\Omega) \approx \pm 1$ kcal/mol (which would explain the different curvatures of the ΔA profiles near *cis*-NMA), while that of the C22 curves is only ± 0.2 kcal/mol (Appendix A), and finite-size effects are negligible, based on tests performed¹⁰ with C22 NMA(aq) in 27 versus 232 H₂O molecules.

Both ΔE_0 and ΔA are a sensitive function of the model physics near the barrier maximum, suggesting that the barrier height is determined primarily by energetic (rather than entropic) factors. The entropic change, $-T\Delta S$, is calculated from the C22 NMA(g) profiles of ΔA and of ΔE , the latter of which is determined both by binning it as a function of Ω and by calculating it from two ΔA curves obtained at 320 and 282 K, according to

$$\Delta E(\Omega; 300 \text{ K}) \approx \frac{\ln \Delta A(\Omega; 282 \text{ K}) - \ln \Delta A(\Omega; 320 \text{ K})}{2\Delta\beta} \quad (3)$$

which is derived from $E(\Omega; 300 \text{ K}) = \partial[\beta A(\Omega)]/\partial\beta$, where $\Delta\beta$

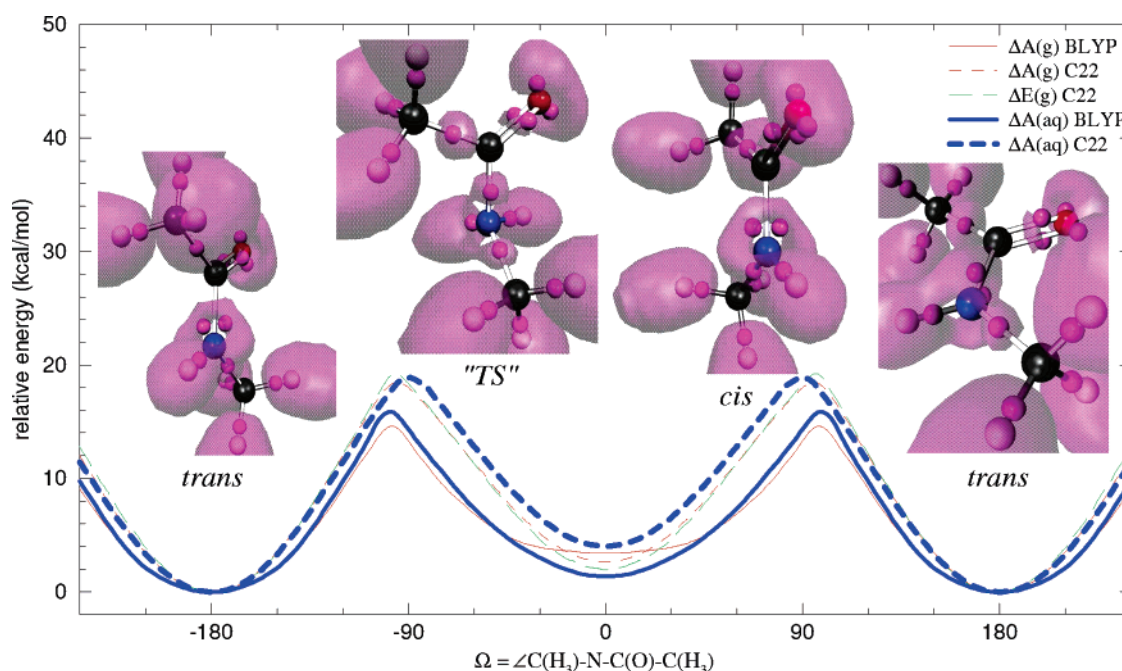


Figure 12. Thermodynamic energy of either NMA(g) or NMA(aq) in 27 H₂O molecules during isomerization and accompanying electronic structure changes (ELF[ρ] = 0.91 = purple isosurface, WFC = small purple spheres that each carry $-2e$ charge, 2° bin).

$= -65.79 \text{ au}^{-1}$. In either case, the C22 NMA(g) profile of $-T\Delta S$ is a relatively constant function that is statistically different from zero only at the barrier maximum and near $\Omega \approx 0^\circ$. The origin, or molecular basis, of this change is examined in Appendix B by defining new thermodynamic functions that can be simply and physically interpreted at the molecular level, for any model system.

B. Geometry of NMA(aq) during Isomerization. The free energy difference between ab initio (BLYP) and empirical (C22) models near the barrier maximum is attributed to a combination of factors. The C22 barrier height is parametrized to a single experimental estimate based on NMR measurements.¹⁹ In contrast, given the excellent agreement between the BLYP/70 Ry and MP2/6-311++G(d,p) ΔE_0 profiles (Figure 11), it is unlikely that AIMD (BLYP/pw) is greatly underestimating the barrier height, which can happen in systems where van der Waals forces are dominant. In fact, the AIMD (BLYP/pw) barrier maximum is lowered in both gas and aqueous phases relative to C22 (Figures 11 and 12) by geometric distortions that are allowed under BLYP but are essentially prohibited under C22.

The geometric changes accompanying isomerization are all localized near the amide nitrogen atom. In Figure 13, selected geometric parameters of NMA(aq) as a function of Ω predicted by both AIMD (BLYP/pw) and C22, obtained by binning the geometry and averaging the results in a given bin, are compared. Three bond lengths and three bond angles, all involving nitrogen, are significantly distorted by more than 0.025 \AA or 1° , respectively, from their equilibrium values during the isomerization of BLYP NMA(aq) (Figure 13) or NMA(g) (not shown). For clarity, only the statistical uncertainty (Appendix A) in the AIMD (BLYP/pw) results is shown; that of C22 is very similar. Conversely, bonds are essentially unchanged and bends are only moderately altered during the C22 simulations (Figure 13). In particular, the BLYP C(O)–N bond is lengthened by 0.1 \AA . The electronic structure changes¹⁰ accompanying this bond elongation are explored in detail in the next section.

C. Electronic Structure of the Amide Group and Peptide Bond in NMA during Isomerization. In this work, as in a previous study,¹⁰ two complementary, state-of-the-art tools are employed to probe the electronic structure of NMA. First, the average position of the electron pairs (in a spin-paired calculation) is provided by the Wannier or Boys–Foster function centers,⁴¹ WFC_{*i*}, which are defined with respect to the expectation value of $N_e/2$ maximally localized orbitals, $\tilde{\phi}_i$:

$$\text{WFC}_i = \langle r_i \rangle = \langle \tilde{\phi}_i | r | \tilde{\phi}_i \rangle \quad (4)$$

The $\tilde{\phi}_i$ are obtained from the AIMD (BLYP/pw) Kohn–Sham orbitals, ϕ_i , via a unitary transformation,

$$\tilde{\phi}_i = \sum_{j=1}^{N_e/2} U_{ij} \phi_j \quad \text{where } \langle \tilde{\phi}_i | \tilde{\phi}_j \rangle = \delta_{ij} \quad (5)$$

and the matrix elements, U_{ij} , are chosen to minimize the spread,

$$S = \sum_{i=1}^{N_e/2} [\langle \phi_i | r^2 | \phi_i \rangle - \langle \langle \phi_i | r | \phi_i \rangle \rangle^2] \quad (6)$$

The second tool, the electron localization functional,⁴² ELF[ρ] or simply ELF, is used to depict regions where electron pair formation is likely and is defined by

$$\text{ELF}[\rho] = \frac{1}{1 + f[\rho, \nabla \rho]} \quad (7)$$

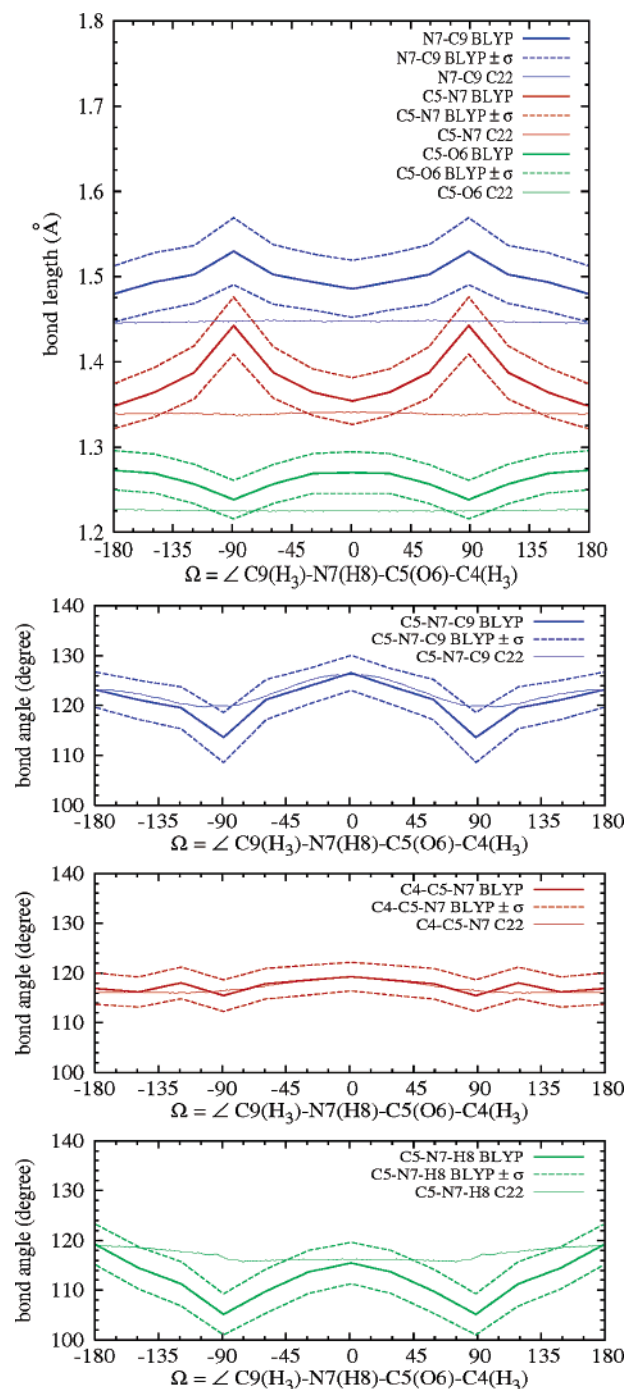


Figure 13. Selected geometric parameters of NMA(aq) in 27 H₂O molecules along the reaction pathway, Ω . The atom indices in the key are defined in the x-axis label.

where $f[\rho, \nabla \rho]$ is related to the probability of a nearby like-spin electron, and $0 \leq \text{ELF}[\rho] \leq 1$. This quantity does not depend on U_{ij} , whose form is arbitrary, but only on the electron density, $\rho(r)$, and its gradient, $\nabla \rho(r)$, and thus offers a check of the Wannier predictions.

Using these tools, a new perspective on the electronic structure of the amide group is gained.¹⁰ In *trans*-NMA or *cis*-NMA, the C(O)–N bond is described by two shared electron binding pairs (BP) (versus lone pairs, LP) lying outside of the molecular plane and forming an angle of $\angle \text{BP}(1)\text{--N--BP}(2) = 70^\circ$ (Figure 12). This strange angular value is explained by the character of either the Wannier orbitals themselves, or the banana-shaped ELF isosurface, which can be thought of as a linear combination of a “bent” nitrogen p_z orbital (due to its

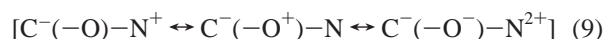
attraction to the positive C(O) nucleus) and a sp_2 hybrid orbital. Conversely, a value of 90° would be predicted assuming a “straight” p_z orbital. Based on static ($T = 0$ K) calculations performed at the same (BLYP/pw) level of theory, this angle is larger than either $\angle BP-C-BP = 50^\circ$ describing the double bond in ethene or $\angle BP-O-BP = 56^\circ$ describing the C=O bond in acetone, because the BP are situated much closer to nitrogen than to carbon in NMA. This fact is a consequence of the octet rule: The neutrality of the carbon atom, with five electron pairs “loosely” associated with it, must be preserved based on linear interpolation of charge population. The structure of the carbonyl bond, with $\angle BP-O-BP = 60^\circ$ and $\angle LP-O-LP = 140^\circ$, is similarly explained. However, the ELF isosurface associated with this bond is noticeably different from that of the partial-double C(O)–N bond (Figure 12).

During isomerization, the peptide C(O)–N bond is significantly altered, whereas the carbonyl bond is essentially unchanged, supporting the Wiberg model of isomerization. The banana-shaped C(O)–N bond is noticeably asymmetric even for a value of $\Omega = \pm 179^\circ$, and, as shown in Figure 12, it is not present near the barrier maximum. Instead, the value of $\angle BP-N-BP$ or $\angle LP-N-BP$ is close to 107.5° , the sp_3 trigonal pyramidal angle in VSEPR theory. On the other hand, the C=O bond, and its associated angles, are essentially unchanged. Thus, the isomerization process is most closely described by the Wiberg model of the amide group, in which only the C(O)–N bond order is affected (or a C \rightarrow N atomic charge transfer is effected) upon converting to the “transition-state” structure, C(=O)–N.

This intuitive pictorial description is complementary to that provided by ab initio valence bond calculations of formamide. As suggested by these calculations,⁹ several resonance forms are needed to describe the planar amide group of *trans*- or *cis*-NMA, three of which are:



while additional forms include



Under a valence bond description, *trans*- or *cis*-NMA can be described by a N \rightarrow C charge transfer and a partial-double C(O)–N peptide bond superimposed on a polarized C=O group. At the barrier maximum, π -electron resonance is inhibited by the molecular conformation (but possibly the N-atom lone pair is slightly delocalized due to hyperconjugation involving the σ frame), and the N-atom is pyramidalized from sp_2 to sp_3 ground states. The former effect is destabilizing and, very likely, only partially offset by the latter, resulting in a significant contribution to the calculated rotational barrier. The length of the C=O bond, a polar entity, in formamide is relatively unchanged.

Our MP2/6-311++G(d,p) calculations can also be reconciled with the above perspectives (as seen in the study of formamide⁹). At the stationary point where $\Omega = 173^\circ$, the calculated C=O and C(O)–N bond populations are 2.64 and 2.28 electrons, respectively, corresponding to bond orders of 1.32 and 1.14. A partial excess electron is included in the O-atom valence shell ($2.68e$). Also, the lone pair of nitrogen is depleted, $1.31e < 2e$, from which mesomeric structure weights of 0.66 (neutral) and 0.34 (zwitterion) are calculated. The expected populations are gradually recovered as the “transition state” is approached, except that the C=O bond population, $\approx 2.4e$, is skewed low due to the electronegativity of oxygen.

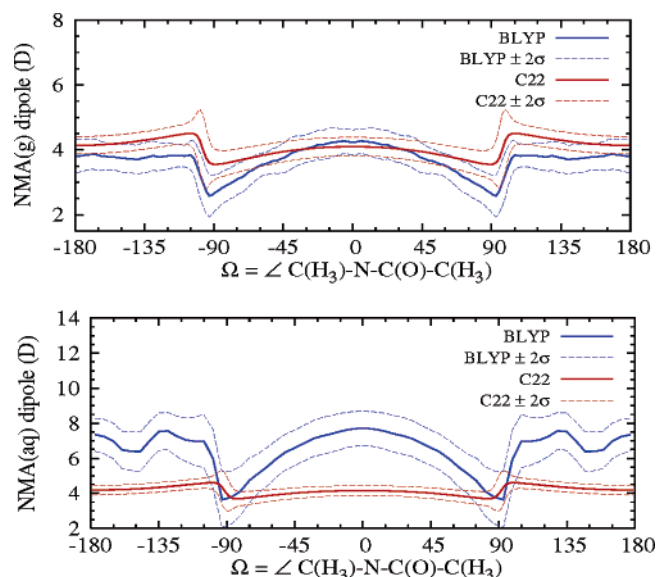


Figure 14. Calculated dipole moment of either (top) NMA(g) (BLYP and C22 results: 2° bin) or (bottom) NMA(aq) in 27 H₂O molecules (BLYP: 6° bin, C22: 2° bin).

D. Molecular Dipole Moment of NMA and Solvating H₂O

Molecules. Although the dipole moment of *trans*-NMA(g) is captured reasonably well by either AIMD (BLYP/pw) or C22, its dependence on the Ω torsion is a sensitive function of the model chosen (Figure 14). This quantity is calculated as a function of Ω by treating each WFC as a charge of $-2e$, assigning positive charges to the atomic nuclei, and averaging either the 5–15 (BLYP) or several thousand (C22) values obtained in a given bin, enabling a direct calculation of the standard deviation (Appendix A). Under BLYP, the dipole moment of *cis*-NMA(g) is a few tenths of a Debye larger than that of *trans*-NMA(g), as predicted by others,⁴³ whereas the converse is true under C22. Also, near the barrier maximum, the profiles are quite different: The shape of the BLYP profile is less symmetric than that of C22, and the drop is more substantial. Although the spread of values obtained in each bin is larger under C22 than under BLYP due to the greater number of configurations sampled, the calculated Ω -dependent error bars are very similar (Figure 14).

In solution, the dipole moment of AIMD (BLYP/pw) NMA(aq) is generally enhanced by a factor of roughly 2, whereas that of C22 NMA(aq) is hardly changed (Figure 14). (Note, 15 BLYP configurations are evaluated in each larger bin.) This approximate doubling⁴³ is due to the electronic polarization of BLYP NMA(aq) accompanied by geometric distortions from hydrogen bonding. Although the average value obtained for configurations with $\Omega \approx 150^\circ$ is nearly 1 D less than that calculated for *trans*-NMA(aq), this likely artifact is within the sampling error. Conversely, the profile describing C22 NMA(aq) is only shifted upward by a small amount relative to that of the gas phase, due to minor geometric perturbations resulting from the NMA-solvent interactions and no polarization effects, because the empirical (atomic) charges are fixed.

The dipole moment of AIMD (BLYP/pw) H₂O molecules in the first solvation shell is different from that of the bulk, whereas it is constant, 2.35 D, under C22 due to the rigidity of the monomer and its static charges. As shown in Figure 15, the dipole moment of AIMD (BLYP/pw) H₂O molecules forming a hydrogen bond to the carbonyl oxygen at an oxygen–oxygen distance of about 2.5 Å is increased by 0.5 D relative to that of other molecules. On the other hand, the dipole moment of H₂O

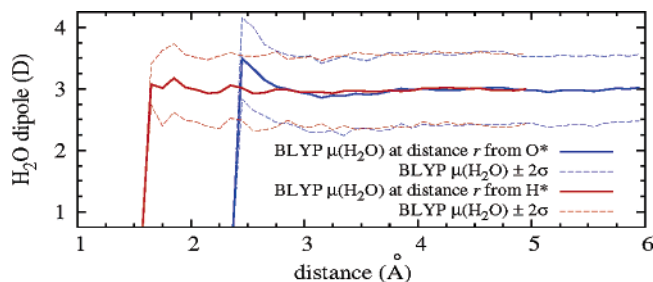


Figure 15. Dipole moment of BLYP H₂O molecules versus distance from either the carbonyl oxygen, O*, or amide hydrogen, H*, of BLYP NMA(aq) (0.1 Å bin).

molecules accepting a hydrogen bond from the amino hydrogen is only slightly enhanced by 0–0.2 D at short distances. The H₂O molecules that are in close proximity to either O*, highly electronegative, or H* are more likely to form a relatively strong hydrogen bond with these bonding partners, resulting in electronic polarization and, likely, the geometric distortion of these H₂O molecules (in the first solvation shell). As expected, far from either the O* or H* atoms, the molecular dipole moment of the BLYP H₂O molecules converges to the previously reported value of 3.0 D in bulk liquid water.⁴⁴

VIII. Conclusions

A detailed examination of the solvent shell structure of NMA(aq) has been performed. Several new predictions were made that are awaiting experimental or theoretical verification. In particular, the carbonyl oxygen–water hydrogen bond is comparable to that in pure liquid water; the CHARMM22 model is predicting a shorter bond, whereas the ab initio (BLYP/pw) treatment is suggesting a slightly longer bond. Both models are unambiguously predicting an amide hydrogen–water oxygen hydrogen bond that is longer than water’s. The rearrangement of solvent molecules within the first shell is comparatively minor during isomerization. Thus, the coupling of solvent degrees of freedom to the reaction coordinate might not dramatically affect the rate of isomerization, in particular, if the solvent rearrangement is fast relative to the comparatively slow isomerization process about the preselected pathway. However, we emphasize that a reaction rate is not computed in this work. Our goal is, rather, the characterization of a *possible* reaction path.

The isomerization process itself is dominated by energetic, and not entropic, contributions, based on a detailed analysis of the thermodynamic changes. The significant difference in predicted barrier heights is attributed to structural deformations near the barrier maximum that are not effectively captured by the CHARMM22 model, resulting from electronic structure changes under the ab initio (BLYP/pw) treatment that are confined primarily to the amide group. Thus, care must be taken when employing empirical models to study processes along the reaction coordinate where the model is not parametrized. As predicted by both models, the entropy change during isomerization is small. An analysis employing CHARMM22 (Appendix B) suggests that the “reaction” is entropically disfavored due to the close proximity of the methyl groups in *cis*-NMA, inhibiting their rotation and anharmonic effects. The details of the electronic structure changes accompanying isomerization are not yet clear, underscoring the need for additional experimental and high-level theoretical studies of the amide group. Note that if atomic charge populations, bond orders, and/or bond orbitals are calculated, their definitions must be consistent with earlier work to ensure a valid comparison.

Acknowledgment. This research was partially supported by NSF (award no. 0229959) and IBM Research (G.J.M. and

Y.A.M.), and R.I. wishes to thank the Natural Science and Engineering Research Council of Canada for a postdoctoral fellowship. We thank Professor Michael L. Klein (University of Pennsylvania) for administering the NSF funds, Drs. Thomas Theis, Mark B. Ketchen, and Yuhai Tu (IBM) for providing office space and computer time on IBM PowerPC 2, 3, and 4 machines, and Professor Jason Crain (University of Edinburgh and IBM) for helpful discussions. Calculations were also performed on the NSF Terascale Computing System (Lemieux) at the Pittsburgh Supercomputing Center. Gaussian 98 computations were carried out on an IBM PowerPC 4 computer at the computer center of IDRIS, Orsay, France. Some figures were prepared using MOLEKEL⁴⁵ and VMD.⁴⁶

Supporting Information Available: The complete citations of refs 14 and 19, a supplementary error analysis, and a tabulation of the functions plotted in Figures 1, 2, 4, 5, 11, 12, 14, and 15. This material is available free of charge via the Internet at <http://pubs.acs.org>.

Appendix A: Error Analysis

In this work, careful attention is paid to the statistical uncertainty associated with the AIMD (BLYP/pw) results. Finite size effects are estimated by comparing results from simulations with C22 NMA(aq) in 27 or 232 H₂O molecules.

The error bars, $\sigma(r)$, given in Figures 1 and 2 and the error bars, $\sigma(\theta)$, in Figures 4 and 5 that bracket the C22 results are actually used to provide an estimate of the error in the AIMD (BLYP/pw) results.¹⁰ These error bars are calculated by first performing several ($N_{\text{sim}} = 20$) C22 simulations with the same system size, $N_{\text{H}_2\text{O}}$, time step, δt , and data collection period, \mathcal{T} , employed in the AIMD (BLYP/pw) simulations. Subsequently, the twenty $g(r)$ values (section III) or $P(\theta)$ values (section V) obtained from these C22 simulations are averaged, enabling the calculation of either $\sigma(r)$ or $\sigma(\theta)$, which are *not* shown on the AIMD (BLYP/pw) results due to the different shapes of the C22 and AIMD (BLYP/pw) functions plotted. The corresponding error in the C22 $g(r)$ itself, calculated from the trajectory of length, $N_{\text{sim}}\mathcal{T}$, is $\sigma_{\text{C22}}(r) = \sigma_m(r) = \sigma(r)/\sqrt{N_{\text{sim}}}$. A similar formula is used to estimate the error in the C22 $P(\theta)$ and may also be applied to estimate the uncertainty from C22 simulations of different arbitrary length.

Both statistical uncertainty and finite-size effects associated with the AIMD (BLYP/pw) 3D maps in section VI are estimated by comparing results from a C22 simulation with the same $N_{\text{H}_2\text{O}}$, δt , and \mathcal{T} , used in the AIMD (BLYP/pw) simulation to those from the “converged” C22 eq-NMA(aq) run employing 232 H₂O molecules. In all cases, the differences between the maps are quite minor, even beyond half the box length, $L/2$, partly due to the understructuring of C22 in this region beyond the first solvation shell. Note that because very long runs would be required to achieve full convergence because of their high dimensionality, the 3D functions are smoothed by applying a moving window average [Savitzky–Golay (0,2,2) filter] first to the cosine terms at every distance (or r value) greater than 2.5 Å and then to these distances at each cosine value. This filtering procedure is applied once to the empirical model results and twice to the AIMD (BLYP/pw) model results in section VI.

The statistical error in the AIMD (BLYP/pw) free energy profiles of Figure 12 is computed as a function of the Ω torsion using the following procedure. Several ($N_{\text{sim}} = 20$) C22 runs are performed with the AIMD (BLYP/pw) $N_{\text{H}_2\text{O}}$, δt , and \mathcal{T} simulation parameters, and $N_{\text{sim}} = 20$ energy profiles are calculated. Each of the C22 curves, $\Delta A_m(\Omega)$, $m = 1, \dots, N_{\text{sim}}$,

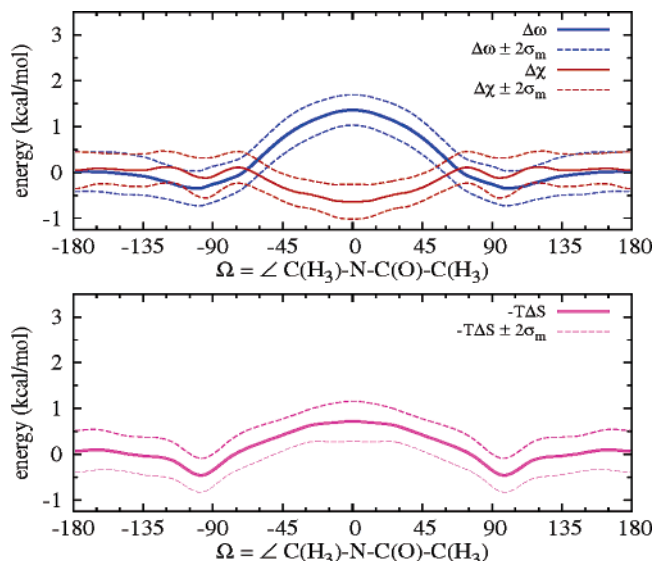


Figure 16. Some thermodynamic quantities of C22 NMA(g). The $-T\Delta S$ curve is the sum of $\Delta\omega$ and $\Delta\chi_e$ curves (2° bin).

which are determined up to an arbitrary constant, is then shifted by a δA_m , chosen to minimize

$$F = \sum_{k,j=1}^{N_{\text{sim}}} \sum_{i=1}^{N_{\text{pnt}}} [\Delta A_k(\Omega_i) - \Delta A_j(\Omega_i) - \delta A_k + \delta A_j]^2 \quad (10)$$

with respect to the δA_m 's. The general solution is

$$\delta A_m = \overline{\Delta A_m} - \overline{\Delta A} + \sum_{j=1}^{N_{\text{sim}}} \delta A_j \quad (11)$$

which can be simplified to

$$\delta A_m = \overline{\Delta A_m} - \overline{\Delta A} \quad (12)$$

if the condition $\sum_{j=1}^{N_{\text{sim}}} \delta A_j = 0$ is imposed, where the mean value of a curve is $\overline{\Delta A_m} = (1/N_{\text{pnt}}) \sum_{i=1}^{N_{\text{pnt}}} \Delta A_m(\Omega_i)$, and the average of the mean values is $\overline{\Delta A} = (1/N_{\text{sim}}) \sum_{j=1}^{N_{\text{sim}}} \overline{\Delta A_j}$. After the twenty δA_m 's are applied to the free energy profiles, $\sigma(\Omega)$ is computed.¹⁰

The Ω -dependent error bars, $\sigma(\Omega)$, in Figures 13, 14, and 15 are calculated straightforwardly. For either the AIMD (BLYP/pw) or C22 simulations, the values of the structural parameters or dipole moment collected in a given bin are averaged, enabling the calculation of $\sigma(\Omega)$.

The Ω -dependent error bars, $\sigma_m(\Omega)$, in Figure 16 provide a direct estimate of the error in the C22 $\Delta\omega$ and $\Delta\chi_e$. After calculating $\sigma(\Omega)$ from several ($N_{\text{sim}} = 20$) C22 simulations with the AIMD (BLYP/pw) $N_{\text{H}_2\text{O}}$, δt , and \mathcal{T} simulation parameters as described above, the desired uncertainty, $\sigma_m(\Omega) = \sigma(\Omega)/\sqrt{N_{\text{sim}}}$, is estimated.

Appendix B: Decomposition of the Entropy Change during a Reaction

The physical basis for the entropic change of a process, $-T\Delta S$, is often difficult to identify. In this section, two new thermodynamic functions are postulated and then analyzed within a rigid rotor-harmonic oscillator model with a weak anharmonic perturbation to gain insight into the entropy change of reaction.

Two new thermodynamic functions are defined in terms of the Helmholtz free energy, ΔA , the energy, ΔE , and the minimum energy, ΔE_o , profiles along the reaction coordinate

$$\begin{aligned} -T\Delta S &= \Delta\omega + \Delta\chi_e \\ \Delta\omega &\equiv \Delta A + \Delta E - 2\Delta E_o \\ \Delta\chi_e &\equiv -2(\Delta E - \Delta E_o) \end{aligned} \quad (13)$$

The new terms split $-T\Delta S$ into two contributions, to which physical meaning can be more easily assigned than to the sum, at least within a model Hamiltonian.

To interpret $\Delta\omega$ and $\Delta\chi_e$, a classical rigid rotor-harmonic oscillator model with an anharmonic perturbation, $\delta\phi$, applied to the harmonic potential, $\phi = (1/2)\sum_i^{3N-7} \mu_i \omega_i^2 S_i^2$, is defined.

$$\delta\phi = \sum_{j,k}^{3N-7} (2 + 4\delta_{jk})^{-1} C_{jk} (\mu_j \omega_j S_j^2) (\mu_k \omega_k S_k^2) \quad (14)$$

Here the C_{jk} are anharmonic coupling constants, and μ_j , ω_j , and S_j are the mass, frequency, and coordinates of the bath modes (i.e., the $3N - 7$ normal modes orthogonal to the reaction coordinate, R), and δ_{jk} is the Kronecker delta. The partition function, $Q_{\text{vib}}^{\text{PE}}$, is straightforwardly calculated within first-order thermodynamic perturbation theory from the total potential, $\phi + \delta\phi$, ultimately yielding eq 15 (where $\beta = 1/kT$).

$$\begin{aligned} Q_{\text{vib}}^{\text{PE}} &= e^{-\beta E_o(R)} \prod_i^{3N-7} \sqrt{\frac{2\pi}{\beta \mu_i \omega_i^2}} \left(1 - \frac{1}{2\beta} \sum_{j,k}^{3N-7} C_{jk} \right) \\ Q_{\text{vib}}^{\text{KE}} &= \prod_i^{3N-7} \sqrt{\frac{\mu_i}{2\pi\hbar^2\beta}} \\ Q_{\text{vib}} &= e^{-\beta E_o(R)} \prod_i^{3N-7} (\beta\hbar\omega_i)^{-1} \left(1 - \frac{1}{2\beta} \sum_{j,k}^{3N-7} C_{jk} \right) \end{aligned} \quad (15)$$

For processes such that $\ln Q(R_{\text{final}}) - \ln Q(R_{\text{init}}) \approx \ln Q_{\text{vib}}(R_{\text{final}}) - \ln Q_{\text{vib}}(R_{\text{init}}) \equiv \ln Q_{\text{vib}}^{(\text{f})} - \ln Q_{\text{vib}}^{(\text{i})}$, e.g., where the molecule's rotational constants can be assumed to be approximately invariant, expressions for the thermodynamic quantities, ΔA and ΔE , can be derived from eq 15 and the relations $A = -\ln Q/\beta$ and $E = -\partial(\ln Q)/\partial\beta$. Substituting the expressions derived for ΔA and ΔE into eq 13 and using the fact that $\omega_j = 1/(\sigma_j\sqrt{\mu_j})$ yields

$$\begin{aligned} \Delta\omega &= \frac{1}{\beta} \sum_j^{3N-7} \ln \left(\frac{\sigma_j^{(\text{i})} \sqrt{\mu_j^{(\text{i})}}}{\sigma_j^{(\text{f})} \sqrt{\mu_j^{(\text{f})}}} \right) \\ \Delta\chi_e &= \frac{1}{\beta^2} \sum_{j,k}^{3N-7} \Delta C_{jk} \end{aligned} \quad (16)$$

where $\Delta C_{jk} = C_{jk}(R_{\text{final}}) - C_{jk}(R_{\text{init}}) \equiv C_{jk}^{(\text{f})} - C_{jk}^{(\text{i})}$.

Making the additional assumptions that the inverse mass tensor in the Cartesian basis is both diagonal and not a function of the reaction coordinate, the product of all the normal mode masses

$$\sum_j^{3N-7} \ln \sqrt{\mu_j} = \frac{1}{2} \ln \prod_j^{3N-7} \mu_j \quad (17)$$

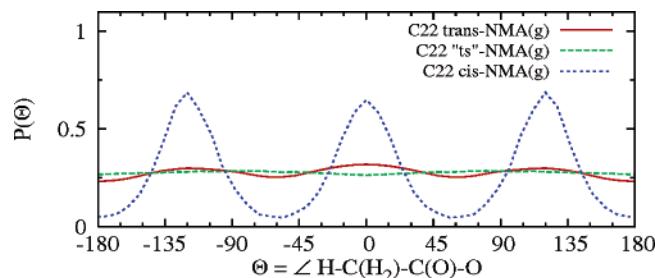


Figure 17. The $\angle\text{H-C(H}_2\text{)-C(O)-O}$ distribution of C22 *trans*-NMA(g) ($\Omega_j = -180^\circ$), “TS”-NMA(g) ($\Omega_j = -90^\circ$), and *cis*-NMA(g) ($\Omega_j = 0^\circ$).

is constant, and eq 16 simplifies to

$$\Delta\omega = \frac{1}{\beta} \sum_j^{3N-7} \ln \frac{\sigma_j^{(i)}}{\sigma_j^{(f)}} \quad (18)$$

$$\Delta\chi_e = \frac{1}{\beta^2} \sum_{j,k}^{3N-7} \Delta C_{jk}$$

Equation 18 is the key result. Provided that the normal mode masses, μ_j , remain essentially unperturbed (e.g., the direction of the modes is constant), $\Delta\omega$ depends only on the widths of the (Gaussian) modal distribution functions, σ_j , at initial and final points along R . Within the model, $\Delta\omega$ becomes a measure of normal mode compression/expansion. In contrast, $\Delta\chi_e$ gives an indication of changes in anharmonicity of the bath modes. The multim minima generalization of this interpretation of eq 13 follows straightforwardly via an inherent structures approach.⁴⁷ Note that many widely used software packages make a strictly harmonic evaluation of $\Delta\omega$ with $\Delta\chi_e = 0$, while the generalized Langevin equation (GLE) assumes a harmonic bath with $\Delta\omega = \Delta\chi_e = -T\Delta S = 0$. These models miss subtle contributions to the entropy changes.

Determining $\Delta\omega$ and $\Delta\chi_e$ for NMA along $R = \Omega$ allows the molecular basis for $-T\Delta S$ to be revealed. For example, relative to *trans*-NMA(g), $\Delta\omega$ under C22 is positive near *cis*-NMA(g) but negative near the barrier maximum (Figure 16). The latter is correlated with changes in the width of methyl H’s torsional distributions (Figure 17). Changes in $\Delta\chi_e$ are observed wherever the molecule’s geometry is distorted from that of *trans*-NMA(g). Thus, the entropy of *cis*-NMA(g) decreases (i.e., $-T\Delta S$ is positive), because the methyl rotation is sterically hindered by the close proximity of methyl groups and anharmonic effects. Conversely, the entropy change near the “transition state” is slightly positive because of facile methyl rotation due to a lack of steric interference. Note that the amide hydrogen, H*, is artificially restrained in the C22 model of NMA,^{19,33,48} and the width of the $\angle\text{H-N-C(O)-C(H}_3\text{)}$ distribution is approximately constant. This latter result is not valid for the ab initio (BLYP) model for which the statistical error in $\Delta\omega$ and $\Delta\chi_e$ is too large, $\pm\sigma = \pm 0.7$ kcal/mol, to permit a meaningful interpretation.

References and Notes

- (1) Creighton, T. E. *Proteins: Structures and Molecular Properties*, 2nd ed.; W. H. Freeman and Company: New York, 1993.
- (2) Guan, R.-J.; Xiang, Y.; He, X.-L.; Wang, C.-G.; Wang, M.; Zhang, Y.; Sundberg, E. J.; Wang, D.-C. *J. Mol. Biol.* **2004**, *341*, 1189–1204.
- (3) Schiene-Fischer, C.; Habazettl, J.; Schmid, F. X.; Fischer, G. *Nat. Struct. Biol.* **2002**, *9*, 419–424.

- (4) Bouckaert, J.; Dewallef, Y.; Poortmans, F.; Wyns, L.; Loris, R. *J. Biol. Chem.* **2000**, *275*, 19778–19787.
- (5) Pal, M.; Dasgupta, S. *Proteins: Struct. Funct. Genet.* **2003**, *51*, 591–606.
- (6) Pappenberger, G.; Aygun, H.; Engels, J. W.; Reimer, U.; Fischer, G.; Kiefhaber, T. *Nat. Struct. Biol.* **2001**, *8*, 452–458.
- (7) Odefey, C.; Mayr, L. M.; Schmid, F. X. *J. Mol. Biol.* **1995**, *245*, 69–78.
- (8) Wiberg, K. B.; Laidig, K. E. *J. Am. Chem. Soc.* **1987**, *109*, 5935.
- (9) For example, Fogarasi, G.; Szalay, P. G. *J. Phys. Chem. A* **1997**, *101*, 1400. Lauvergnat, D.; Hiberty, P. C. *J. Am. Chem. Soc.* **1997**, *119*, 9478. Basch, H.; Hoz, S. *Chem. Phys. Lett.* **1998**, *294*, 117. Quiñero, D.; Frontera, A.; Capó, M.; Ballister, P.; Suñer, G. A.; Garau, C.; Deyá, P. M. *New J. Chem.* **2001**, *25*, 259. Mo, Y.; Schleyer, P. v. R.; Wu, W.; Lin, M.; Zhang, Q.; Gao, J. *J. Phys. Chem. A* **2003**, *107*, 10011.
- (10) Mantz, Y. A.; Gerard, H.; Ifimie, R.; Martyna, G. J. *J. Am. Chem. Soc.* **2004**, *126*, 4080–4081.
- (11) Car, R.; Parrinello, M. *Phys. Rev. Lett.* **1985**, *55*, 2471.
- (12) Ifimie, R.; Minary, P.; Tuckerman, M. E. *Proc. Natl. Acad. Sci. U.S.A.* **2005**, *102*, 6654–6659.
- (13) Tuckerman, M. E.; Yarne, D. A.; Samuelson, S. O.; Hughes, A. L.; Martyna, G. J. *Comput. Phys. Commun.* **2000**, *128*, 333–376.
- (14) Frisch, M. J. et al. *Gaussian 98*, revision A.11; Gaussian, Inc.: Pittsburgh, PA, 2001.
- (15) Becke, A. *Phys. Rev. A* **1988**, *38*, 3098. Lee, C.; Yang, W.; Parr, R. G. *Phys. Rev. B* **1988**, *37*, 785.
- (16) Mantz, Y. A.; Chen, B.; Martyna, G. J. *J. Phys. Chem. B* **2006**, *110*, 3540–3554.
- (17) Nosé, S. *Mol. Phys.* **1984**, *52*, 255. Hoover, W. G. *Phys. Rev. A* **1985**, *31*, 1695. Martyna, G. J.; Tuckerman, M. E.; Klein, M. L. *J. Chem. Phys.* **1992**, *97*, 2635.
- (18) Tassone, F.; Mauri, F.; Car, R. *Phys. Rev. B* **1994**, *50*, 10561–10573.
- (19) MacKerell, A. D., Jr. et al. *J. Phys. Chem. B* **1998**, *102*, 3586.
- (20) Jorgensen, W. L.; Chandrasekhar, J.; Madura, J. D.; Impey, R. W.; Klein, M. L. *J. Chem. Phys.* **1983**, *79*, 926–935.
- (21) Samuelson, S. O.; Martyna, G. J. *J. Chem. Phys.* **1998**, *109*, 11061–11073.
- (22) Yarne, D.; Tuckerman, M. E.; Martyna, G. J. *J. Chem. Phys.* **2001**, *115*, 3531–3539.
- (23) Martyna, G. J.; Tuckerman, M. E. *J. Chem. Phys.* **1999**, *110*, 2810–2821.
- (24) Li, J.-H.; Allinger, N. L. *J. Comput. Chem.* **1998**, *19*, 1001.
- (25) Because the hydrogen bonds formed in condensed-phase systems can be quite different from those in clusters because of, e.g., large changes in molecular dipole moments and cooperative effects, it is normally ill-advised to apply conclusions from the gas phase to solution. However, for a single H₂O molecule interacting with either the O* or H* atoms in NMA, a shorter and stronger O*–H and a longer and weaker H*–O hydrogen bond, with counterpoise corrected binding energies of $\Delta E_0(\text{CPC}) = 7.0$ and 4.1 kcal/mol, respectively,²⁶ relative to that in the water dimer, with $\Delta E_0(\text{CPC}) = 5.4$ kcal/mol,²⁷ are predicted at the MP2/6-311++G(2d,2p) level of theory, consistent with a separate analysis of the free energy surfaces employing the C22 force field.²⁸
- (26) Langley, C. H.; Allinger, N. L. *J. Phys. Chem. A* **2003**, *107*, 5208–5216.
- (27) Frisch, M. J.; Bene, J. E. D.; Binkley, J. S.; Schaefer, H. F., III. *J. Chem. Phys.* **1986**, *84*, 2279.
- (28) Buck, M.; Karplus, M. *J. Phys. Chem. B* **2001**, *105*, 11000–11015.
- (29) Gao, J.; Freindorf, M. *J. Phys. Chem. A* **1997**, *107*, 3182–3188.
- (30) Svishchev, I. M.; Kusalik, P. G. *J. Chem. Phys.* **1993**, *99*, 3049. Kusalik, P. G.; Svishchev, I. M. *Science* **1994**, *265*, 1219. Svishchev, I. M.; Zassetsky, A. Y.; Kusalik, P. G. *Chem. Phys.* **2000**, *258*, 181.
- (31) Trout, B. L.; Parrinello, M. *J. Phys. Chem. B* **1999**, *103*, 7340.
- (32) Whitfield, T. W.; Martyna, G. J.; Allison, S.; Bates, S. P.; Crain, J. *Chem. Phys. Lett.* **2005**, *414*, 210–214.
- (33) Wei, D.; Guo, H.; Salahub, D. R. *Phys. Rev. E* **2001**, *64*, 011907.
- (34) Luque, F. J.; Orozco, M. *J. Org. Chem.* **1993**, *58*, 6397–6405.
- (35) Han, W.-G.; Suhai, S. *J. Phys. Chem.* **1996**, *100*, 3942–3949.
- (36) Guo, H.; Karplus, M. *J. Phys. Chem.* **1992**, *96*, 7273–7287.
- (37) Cuevas, G.; Renugopalakrishnan, V.; Madrid, G.; Hagler, A. *Phys. Chem. Chem. Phys.* **2002**, *4*, 1490–1499.
- (38) Kang, Y. K. *J. Mol. Struct. (THEOCHEM)* **2001**, *546*, 183–193.
- (39) All initial structures (preceding geometry optimization) were constructed by twisting the most stable *cis*-NMA(g) methyl rotamer about Ω , yielding a *trans*-NMA(g) rotamer that is the most energetically favored by C22 but not by BLYP/70 Ry. Thus, the relative energy of BLYP *cis*-NMA(g) is (slightly) underestimated. Because similar ratios of methyl rotamers were observed in the C22 umbrella sampling simulations for absolute values of greater than 30°, the predicted BLYP/70 Ry barrier height is likely unaffected by this choice. Also, a zero-point energy correction is not included in any results.
- (40) Rick, S. W.; Berne, B. E. *J. Am. Chem. Soc.* **1996**, *118*, 672–679.

- (41) Wannier, G. H. *Phys. Rev.* **1937**, 52, 191. Foster, J. M.; Boys, S. F. *Rev. Mod. Phys.* **1960**, 32, 300. King-Smith, R. D.; Vanderbilt, D. *Phys. Rev. B* **1993**, 47, 1651. Resta, R. *Phys. Rev. Lett.* **1998**, 80, 1800. Berghold, G.; Mundy, C. J.; Romero, A.; Hutter, J.; Parrinello, M. *Phys. Rev. B* **2001**, 61, 10040. Iftimie, R.; Thomas, J. W.; Tuckerman, M. J. *Chem. Phys.* **2004**, 120, 2169.
- (42) Becke, A. D.; Edgecombe, K. E. *J. Chem. Phys.* **1990**, 92, 5397.
- (43) Gaigeot, M. P.; Vuilleumier, R.; Sprik, M.; Borgis, D. *J. Chem. Theory Comput.* **2005**, 1, 772–789.
- (44) Kuo, I.-F. W.; Mundy, C. J. *Science* **2004**, 303, 658. Chen, B.; Ivanov, I.; Klein, M. L.; Parrinello, M. *Phys. Rev. Lett.* **2003**, 91, 215503.
- Silvestrelli, P. L.; Parrinello, M. *Phys. Rev. Lett.* **1999**, 82, 3308. Silvestrelli, P. L.; Parrinello, M. *J. Chem. Phys.* **1999**, 111, 3572.
- (45) Flükiger, P.; Lüthi, H. P.; Portmann, S.; Weber, J. *MOLEKEL 4.0*; Swiss Center for Scientific Computing, Manno, Switzerland, 2000.
- (46) Humphrey, W.; Dalke, A.; Schulten, K. VMD 1.8.2, *J. Mol. Graph.* **1996**, 14, 33.
- (47) Stillinger, F. H.; Weber, T. A. *Phys. Rev. A* **1982**, 25, 978–989.
- (48) Head-Gordon, T.; Head-Gordon, M.; Frisch, M. J.; Brooks, C. L., III; Pople, J. A. *J. Am. Chem. Soc.* **1991**, 113, 5989–5997.